

# JGR Space Physics

## RESEARCH ARTICLE

10.1029/2021JA029191

### Key Points:

- We calculate the flow deflection, electric currents, and plasma and energy flux patterns for sub-Alfvénic moon-magnetosphere interactions
- The number flux of the magnetospheric flow peaks above the obstacle's ramside apex, but the energy flux achieves its minimum in that region
- The currents along the Alfvén wing characteristics exhibit several sharp jumps, generating observable spikes in the magnetic field

### Correspondence to:

S. Simon,  
[sven.simon@eas.gatech.edu](mailto:sven.simon@eas.gatech.edu)

### Citation:

Simon, S., Liuzzo, L., & Addison, P. (2021). Role of the ionospheric conductance profile in sub-Alfvénic moon-magnetosphere interactions: An analytical model. *Journal of Geophysical Research: Space Physics*, 126, e2021JA029191. <https://doi.org/10.1029/2021JA029191>

Received 3 FEB 2021

Accepted 19 JUN 2021

## Role of the Ionospheric Conductance Profile in Sub-Alfvénic Moon-Magnetosphere Interactions: An Analytical Model

Sven Simon<sup>1</sup> , Lucas Liuzzo<sup>2</sup> , and Peter Addison<sup>1</sup> 

<sup>1</sup>School of Earth and Atmospheric Sciences, Georgia Institute of Technology, Atlanta, GA, USA, <sup>2</sup>Space Sciences Laboratory, University of California, Berkeley, CA, USA

**Abstract** We develop an analytical model of the Alfvén wings generated by the interaction between a moon's ionosphere and its sub-Alfvénic magnetospheric environment. Our approach takes into account a realistic representation of the ionospheric Pedersen conductance profile that typically reaches a local minimum above the moon's poles and maximizes along the bundle of magnetospheric field lines tangential to the surface. By solving the equation for the electrostatic potential, we obtain expressions for various quantities characterizing the interaction, such as the number flux and energy deposition of magnetospheric plasma onto the surface, the spatial distribution of currents within the Alfvén wings and associated magnetic field perturbations, as well as the Poynting flux transmitted along the wings. Our major findings are: (a) Deflection of the magnetospheric plasma around the Alfvén wings can reduce the number flux onto the surface by several orders of magnitude. However, the Alfvénic interaction alone does not alter the qualitative shape of the “bullseye”-like precipitation pattern formed without the plasma interaction. (b) Due to the deflection of the upstream plasma, the energy deposition onto the moon's exosphere achieves its minimum near the ramside apex and maximizes along the flanks of the interaction region. (c) Even when the ionospheric conductance profile is continuous, the currents along the Alfvén wings exhibit several sharp jumps. These discontinuities generate spikes in the magnetic field that are still observable at large distances to the moon. (d) The magnitude and direction of the wing-aligned currents are determined by the slope of the ionospheric conductance profile.

### 1. Introduction

The Galilean moons of Jupiter and the largest satellites of Saturn are located within their parent planets' magnetospheres where they are continuously overtaken by a partially corotating plasma flow. The obstacle that a moon represents to this incident magnetospheric plasma can consist mainly of its dense atmosphere and ionosphere, as is the case at Jupiter's volcanic moon Io (Blöcker et al., 2018) and Saturn's largest moon Titan (e.g., Neubauer et al., 1984, 2006; Simon et al., 2015). At Europa, Ganymede, and Callisto the resulting ionosphere-magnetosphere interaction is modified to a varying degree by permanent or induced magnetic moments from the objects' interiors and ionospheres (e.g., Hartkorn & Saur, 2017; Kivelson et al., 1999, 2002; Liuzzo et al., 2016; Zimmer et al., 2000). The neutral gas envelopes of, for example, Saturn's icy moons Tethys, Dione, and Rhea are so dilute that newly produced ions can be treated as test particles and the observed magnetic field perturbations arise almost exclusively from absorption of the impinging magnetospheric flow at the moons' surfaces (e.g., Krupp et al., 2020; Roussos et al., 2008; Simon et al., 2009; Simon, Saur, Kriegel, et al., 2011; Simon, Saur, Neubauer, et al., 2011). If the combination of ambient magnetic field strength, upstream plasma density and temperature is favorable, such an absorption-driven interaction alone may still generate weak Alfvén wings, as observed by the Cassini spacecraft at Rhea (Khurana et al., 2017; Simon et al., 2012). However, the present study focuses on interaction scenarios where the obstacle to the plasma flow is represented mainly by the moon's atmosphere and ionosphere.

The sub-Alfvénic interaction of a moon's ionosphere with the impinging magnetospheric plasma generates two Alfvén wings, that is, a system of non-linear, standing Alfvén waves that connects the moon to its parent planet's polar ionosphere (e.g., Neubauer, 1980, 1998, 1999 and references therein). At distances to the moon where the magnetospheric magnetic field  $B_0$  can still be treated as (approximately) uniform, the plasma and field perturbations associated with these wings exhibit translational invariance along the two

Alfvén characteristics  $\underline{u}_0 \pm \underline{v}_{A,0}$ , where  $\underline{u}_0$  denotes the upstream velocity vector of the unperturbed magnetospheric flow and  $\underline{v}_{A,0}$  represents the Alfvén velocity (Neubauer, 1980). In other words, when looking into the directions of the wing characteristics, the Alfvénic perturbations do *not* fade away with distance from the obstacle. This important property has already been applied to search for, for example, plasma interaction signatures of plumes at Enceladus (Kriegel et al., 2011, 2014; Simon, Saur, Kriegel, et al., 2011; Simon, Saur, Neubauer, et al., 2011) and Europa (Blöcker et al., 2016) in magnetic field data from remote flybys of these moons.

While a broad variety of numerical models have been applied to study sub-Alfvénic moon-plasma interactions at Jupiter (e.g., Arnold et al., 2019; Liuzzo et al., 2016, 2018; Poppe et al., 2018; Rubin et al., 2015) and Saturn (e.g., Krupp et al., 2020; Roussos et al., 2008; Simon et al., 2009), numerous key properties of the Alfvén wings can already be captured through idealized analytical models (i.e., “with paper and pen”). Such analytical solutions of the incompressible magnetohydrodynamic equations are particularly helpful in elucidating the fundamental physical processes involved in a moon’s plasma interaction, such as the dependency of the magnetic field perturbations on key parameters like the Alfvénic Mach number  $M_A$ , the Alfvén conductance  $\Sigma_A$ , or the moon’s ionospheric conductance profile. A first step in this direction was made by Saur et al. (1999): Building upon the original studies of Neubauer (1980, 1998), these authors derived an analytical expression for the electrostatic potential  $\psi$  near Io’s Alfvén wings and applied it to constrain the reduction of the electric field within the wings and the deflection of the upstream plasma flow. In this way, Saur et al. (1999) were able to highlight the importance of asymmetries associated with the ionospheric Hall effect for the interpretation of plasma and magnetic field observations from flybys of Io.

Neubauer (1998) showed that the properties of a moon’s Alfvén wings are determined exclusively by the Pedersen ( $\Sigma_P$ ) and Hall ( $\Sigma_H$ ) conductances (height-integrated conductivities) of its ionosphere. In other words, the flow deflection pattern and the field perturbations near the Alfvén wings are identical for two different ionospheric conductivity distributions, as long as the (height-integrated) conductance profiles are the same. The Pedersen and Hall conductances of a planetary moon’s ionosphere are obtained by integrating the local Pedersen and Hall conductivities along the segments of the magnetospheric field lines that thread the ionosphere (e.g., Saur et al., 1999; Simon, 2015). As illustrated in Figure 6 of Neubauer (1998), Figure 1 of Simon (2015), and Figure 1 of Blöcker et al. (2016), the Pedersen and Hall conductance profiles exhibit a “suspension bridge”-like shape. The values of the conductances assume local minima above the moon’s poles where the magnetospheric field is perpendicular to the surface (assuming the ambient field  $\underline{B}_0$  to point mainly in north-south direction). Both conductances then increase monotonically with radial distance from an axis through the poles and achieve their maxima along the bundle of magnetospheric field lines tangential to the surface of the moon (hereinafter referred to as the “moon’s fluxtube”). At the surface of the moon’s fluxtube, the magnetospheric field lines no longer intersect the solid body. Therefore, the length of the integration path along the field lines is largest, causing a sharp peak in the conductances. Outside of the moon’s fluxtube, the ionospheric conductances typically drop monotonically with distance from the obstacle, due to the decreasing path length of the magnetic field lines within its neutral gas envelope.

In their initial analytical model, Saur et al. (1999) approximated this conductance profile with a piecewise constant function, setting  $\Sigma_P$  and  $\Sigma_H$  to non-vanishing and uniform values within a circular region representing the moon’s ionosphere and to zero outside. While such a “box-like” ionosphere model is highly suitable to identify the cause of any asymmetries in the deflected flow pattern, it also generates an artificial set of rotational discontinuities in the magnetic field at the transition from non-vanishing to zero ionospheric conductance (Saur et al., 2007; Simon, Saur, Kriegel, et al., 2011; Simon, Saur, Neubauer, et al., 2011; Simon, 2015). The occurrence of these artificial magnetic discontinuities is particularly problematic when the interaction between the moon and its magnetospheric environment also involves the formation of actual *physical* jumps in the magnetic field components. A prominent example are the rotational discontinuities generated by plume-plasma interactions at Enceladus (Saur et al., 2007; Simon, Saur, Kriegel, et al., 2011; Simon, Saur, Neubauer, et al., 2011; Simon et al., 2014) and Europa (Arnold et al., 2019; Blöcker et al., 2016; Jia et al., 2018).

The work of Saur et al. (1999) gave rise to a series of follow-up analytical studies that applied piecewise constant ionospheric conductance profiles of successively increasing complexity to investigate various aspects of sub-Alfvénic moon-plasma interactions. By transforming the original equation for the Alfvén wings’

electric potential  $\psi$  to elliptical coordinates, Saur (2004) investigated how the shape of the box-like ionosphere region (circular vs. elliptical) affects the current systems that connect the moon to its parent planet's ionosphere. Subsequently, Saur et al. (2007) modeled the magnetic field perturbations generated by the north-south asymmetry of Enceladus' magnetospheric interaction, caused by the south-polar plume. These authors proposed the existence of – subsequently observed – magnetic discontinuities at the surface of this icy moon's fluxtube. Simon, Kriegel, et al. (2013), Simon, Saur, Kriegel, et al. (2011), and Simon, Saur, Neubauer, et al. (2011) applied a similar analytical approach to constrain the contribution of negatively charged dust grains in the Enceladus plume to the magnetic perturbations observed by the Cassini spacecraft. Their work revealed a reversal in the sign of the Hall conductance  $\Sigma_H$  (and associated magnetic perturbations) once a sufficiently large fraction of the magnetospheric electrons is attached to the dust grains. So far, the most complex iteration of the analytical model with piecewise constant conductances was more recently presented by Blöcker et al. (2016): These authors represented Europa's ionospheric conductance profile as a step function with 11 different levels, thereby mimicking the exponential decrease of  $\Sigma_P$  and  $\Sigma_H$  with distance from the moon's fluxtube. Blöcker et al. (2016) applied their model to identify possible magnetic signatures of plume-plasma interactions in Galileo data from the non-targeted E25A flyby which occurred at a distance of more than six Europa radii. Treating the obstacle to the flow as a “box” with constant Pedersen conductance and zero Hall conductance, Saur et al. (2013) provided a comprehensive analysis of the energy flux transmitted by an exoplanet toward its host star when exposed to a sub-Alfvénic stellar wind.

Simon (2015) searched for an analytical description of the electric potential and the magnetic field perturbations in a moon's Alfvén wings that takes into account a more realistic representation of the continuous, “suspension bridge”-like ionospheric conductance profile. Assuming the ambient magnetospheric field  $B_0$  to point strictly in north-south direction, this author applied a sequence of power laws (with different exponents) to emulate the dependency of the Pedersen conductance  $\Sigma_P(r)$  on the distance  $r$  from an axis through the moon's poles. As demonstrated by Simon (2015), a “pawn sacrifice” is required to find an analytical description of the potential  $\psi$  for a continuous Pedersen conductance profile: The ionospheric Hall conductance needs to be set to  $\Sigma_H \equiv 0$ . This step eliminates any asymmetries in the flow pattern and magnetic field between the moon's planet-facing and planet-averted hemispheres that would otherwise be caused by the ionospheric Hall effect. Thus, if the exosphere and ionosphere do not possess any hemispheric asymmetries, the plasma perturbations caused by the interaction are the same on both sides of the moon. The ionospheric Hall effect was found crucial in interpreting certain aspects of the magnetic field perturbations observed at Io and Enceladus, especially the signatures generated in the field component along the moon-planet line (Kriegel et al., 2011, 2014; Saur et al., 1999; Simon, Saur, Kriegel, et al., 2011; Simon, Saur, Neubauer, et al., 2011; Simon et al., 2014). However, a major advantage of the approach of Simon (2015) is that – since the ionospheric conductance profile is continuous everywhere – the model does *not* produce any artificial discontinuities in the magnetic field.

Simon (2015) applied their model to study the *hemisphere coupling effect* at Enceladus, that is, the currents on the surface of the moon's fluxtube that stem from the partial reflection of the northern Alfvén wing (generated by the Enceladean south-polar plume) at the moon's non-conducting icy surface. However, the approach of Simon (2015) is far more suitable at, for example, Europa where the ionospheric Pedersen conductance clearly exceeds the Hall conductance (Kivelson et al., 2004) and the notion of a symmetric flow pattern is more adequate. In addition, their study focused entirely on establishing upper limits for the magnitude of the surface currents and the strength of the associated discontinuities in the magnetic field. Other important quantities, such as the flow pattern, the spatial distribution of the plasma flux onto Enceladus' surface, or the Poynting flux radiated away by interaction, were not discussed. However, the analytical approach provides straightforward access to these quantities as well, allowing to easily constrain their dependency on the parameters of the upstream flow and the obstacle. This is particularly important since the output of *numerical* models of moon-magnetosphere interactions is, to a certain degree, affected by the choice of boundary conditions required to incorporate the solid body of the obstacle into the plasma simulation. Since an analytical approach is not subject to such constraints, it allows to identify fine structures in the plasma flow pattern, current systems, and magnetic field that would otherwise be partially shrouded by the applied boundary conditions or insufficient resolution of the simulation grid.

Building upon the work of Simon (2015), the goal of our study is therefore to determine analytical expressions for important properties of sub-Alfvénic moon-magnetosphere interactions when a continuous ionospheric Pedersen conductance profile is taken into account. In addition to the Alfvén wing currents and associated magnetic perturbations, we shall focus on the deflection pattern of the magnetospheric plasma, the number and energy fluxes of the flow onto the moon’s surface as well as the Poynting flux radiated away along the Alfvén wing characteristics. While we strive to explore the fundamental physics of sub-Alfvénic moon-magnetosphere interactions rather than analyze a specific spacecraft data set, the insights provided by our study should significantly facilitate understanding of in-situ observations from future flybys of Jupiter’s (e.g., during the Europa Clipper or JUpiter ICy moons Explorer [JUICE] missions) and Saturn’s icy moons.

This study is structured as follows: In Section 2, we identify a new class of solutions for the electric potential  $\psi$  near the Alfvén wings. In contrast to the approach of Simon (2015), this type of solution no longer describes the Pedersen conductance  $\Sigma_P(r)$  as a sequence of polynomials, but is based on an *exponential* form of the conductance profile. This approach is, in part, complementary to the work of Blöcker et al. (2016): These authors showed that  $\Sigma_P(r)$  outside of Europa’s fluxtube can be approximated by an exponential profile, but represented it with a piecewise constant function in their analytical calculations. The solution for  $\psi(r)$  is then used to calculate various physical quantities describing the moon-magnetosphere interaction. In Section 3, we present a case study that applies this analytical model to Europa’s interaction with Jupiter’s magnetospheric plasma sheet. The physical mechanisms that shape, for example, the field perturbations and currents, the plasma’s number and kinetic energy flux onto the surface, and the electromagnetic Poynting flux are discussed in detail. Section 4 concludes our study with a brief summary of its major findings.

## 2. Model Description

In this section, we solve the differential equation for the electrostatic potential  $\psi$  near the Alfvén wings for an exponential conductance profile and derive expressions for associated physical quantities. Before going into the mathematical derivation, the underlying assumptions and simplifications of the analytical approach are briefly reviewed in Section 2.1. For a more detailed discussion of the basic principles of this model, the reader is referred to preceding publications from this series cited in the introduction, with the latest update provided in sections 1 and 2 of Simon (2015).

The Cartesian coordinate system applied throughout this work is the *Satellite Interaction System*  $\{x, y, z\}$ , the origin of which is located at the center of the moon. The unit vectors of this coordinate system are referred to as  $\{\underline{e}_x, \underline{e}_y, \underline{e}_z\}$ . The (+x)-axis is aligned with the uniform bulk velocity  $\underline{u}_0 = u_0 \underline{e}_x$  of the magnetospheric upstream plasma. The (+z)-axis points northward. The ambient magnetospheric field  $\underline{B}_0 = -B_0 \underline{e}_z$  is assumed to be uniform and to point southward, that is, it is aligned with the *negative* z-axis. The (+y)-axis completes the right-handed system, pointing toward the moon’s parent planet (assuming an approximately circular orbit). Thus, the unperturbed convective electric field  $\underline{E}_0 = -\underline{u}_0 \times \underline{B}_0 = -u_0 B_0 \underline{e}_y$  is antiparallel to the y-axis. The electric potential  $\psi_0$  in the undisturbed upstream plasma is therefore given by  $\psi_0 = u_0 B_0 y$  and is related to the observable vector quantities of the unperturbed flow through  $\nabla \psi_0 = \underline{B}_0 \times \underline{u}_0$ . We also introduce polar coordinates  $(r, \phi)$  in planes perpendicular to the magnetospheric background field:  $x = r \cos \phi$ ,  $y = r \sin \phi$ , where  $r = \sqrt{x^2 + y^2}$ ,  $\cos \phi = x / \sqrt{x^2 + y^2}$ , and  $\sin \phi = y / \sqrt{x^2 + y^2}$ . The normalized covariant basis vectors of this polar coordinate system are referred to as  $\underline{e}_r$  (radial) and  $\underline{e}_\phi$  (azimuthal), respectively.

### 2.1. Underlying Assumptions and Simplifications

Throughout this study, the obstacle represented by the moon is assumed to consist *exclusively* of its (spatially non-uniform) ionospheric Pedersen conductance  $\Sigma_P(r)$ . We treat the moon as being devoid of any permanent or induced magnetic moment, although such internally generated magnetic fields were observed at Ganymede (Kivelson et al., 2002), Europa, and (likely) Callisto (Liuzzo et al., 2016; Zimmer et al., 2000). Consequences of this assumption are discussed in Section 2.4.

Our analytical model assumes the magnetic field perturbations  $\delta \underline{B}$  associated with the Alfvén wings to be much weaker than the magnetospheric background field  $\underline{B}_0$ . Thus, the Alfvénic Mach number of the

upstream flow needs to fulfill  $M_A \ll 1$ . In this case, the field lines of the magnetospheric background field  $B_0$  (which are aligned with the  $z$ -axis) still approximately coincide with the isolines of the electrostatic potential  $\psi$ . In other words,  $\psi = \psi(x, y)$  depends only on the two coordinates perpendicular to the magnetospheric field, and the electric field can be expressed as

$$\underline{E} = -\nabla\psi(x, y) = -\left\{\frac{\partial\psi}{\partial x}\underline{e}_x + \frac{\partial\psi}{\partial y}\underline{e}_y\right\}. \quad (1)$$

The conductance profile  $\Sigma_p(r)$  of the moon's ionosphere is assumed to be axially symmetric, that is, it depends only on the distance  $r = \sqrt{x^2 + y^2}$  to the  $z$ -axis. In analogy to Simon (2015) we take into account a non-trivial radial dependency of the ionospheric Pedersen conductance to approximate a realistic shape of the "suspension bridge"-like ionospheric conductance profile. However, this happens at the expense of neglecting asymmetries in the flow pattern and magnetic field caused by the Hall effect ( $\Sigma_H = 0$ ).

Also, the model considers only the perturbations generated by the Alfvénic component of the interaction alone, that is, additional (compressional) contributions to the flow deflection and magnetic field through transverse currents in the moon's ionosphere are not taken into account. While the perturbations generated by local current systems near the moon can, in principle, be incorporated into the model formalism, this step can be completed only numerically (Simon, Saur, Kriegel, et al., 2011; Simon, Saur, Neubauer, et al., 2011). Thus, the model would lose its major advantage over magnetohydrodynamic or hybrid plasma simulation codes that can readily accommodate a way more detailed (but less accessible) description of the involved physics. However, we will revisit this simplification in Section 2.4.

## 2.2. Governing Equations

Treating the Alfvénic interaction as symmetric between the moon's planet-facing ( $y > 0$ ) and planet-averted ( $y < 0$ ) hemispheres, Simon (2015) showed that the electric potential can be expressed as  $\psi(r, \phi) = \Lambda(r)\sin\phi$ , where the radial component  $\Lambda(r)$  can be obtained from the ordinary differential equation

$$-\frac{1}{r^2}\Lambda(r) + \left[\frac{1}{r} + \frac{d}{dr}\ln(\Sigma(r))\right]\frac{d\Lambda(r)}{dr} + \frac{d^2\Lambda(r)}{dr^2} = 0 \quad (2)$$

with  $\Sigma(r) \equiv \Sigma_p(r) + \Sigma_A$ , see Equations 17–20 in that work. The parameter

$$\Sigma_A = \frac{1}{\mu_0 v_{A,0} \sqrt{M_A^2 + 1}} \quad (3)$$

is the Alfvén conductance (see Neubauer, 1980). At this point, the conductance profile  $\Sigma(r)$  needs to be specified in order to solve for  $\Lambda(r)$ . While Simon (2015) assumed a power law dependency ( $\Sigma(r) \propto r^\kappa$  with a constant exponent  $\kappa$ ), here we develop a new class of solutions that uses an exponential conductance profile:

$$\Sigma(r) = \alpha \exp(\beta r). \quad (4)$$

In this expression,  $\alpha$  and  $\beta$  denote given constants. While the properties of the resulting solution for  $\psi(r, \phi)$  are qualitatively similar to those described in Simon (2015), having a second, independent class of solutions available for  $\psi(r, \phi)$  provides additional degrees of freedom in adjusting the model parameters to the specifics of an observed interaction scenario.

Using Equation 4, the expression for the radial part of the potential becomes

$$-\frac{1}{r^2}\Lambda(r) + \left[\frac{1}{r} + \beta\right]\frac{d\Lambda(r)}{dr} + \frac{d^2\Lambda(r)}{dr^2} = 0. \quad (5)$$

As demonstrated in detail in Appendix A, the general solution of this equation can be written as

$$\Lambda(r) = \frac{K_1(\beta r - 1) + K_2 \exp(-\beta r)}{r} \quad (6)$$

with constants of integration  $K_1$  and  $K_2$ . We now apply Equation 4 to emulate the “suspension bridge”-like conductance profile in the ionosphere of a moon of radius  $R_1$ . For this purpose we set

$$\Sigma_P(r) = \begin{cases} (\Sigma_{P,0} + \Sigma_A) \exp(\beta r) - \Sigma_A & ; r \leq R_1 & (\text{region I}) \\ \gamma \exp(-\delta r) - \Sigma_A & ; R_1 < r \leq R_2 & (\text{region II}) \\ 0 & ; R_2 < r & (\text{region III}) \end{cases}, \quad (7)$$

where the constant  $\Sigma_{P,0}$  describes the Pedersen conductivity, integrated exactly along the  $z$ -axis, in one of the moon’s hemispheres (Saur et al., 1999). The positive constant  $\beta$  is a free parameter that can be adjusted to match observations constraining the steepness of the ionospheric conductance profile within the moon’s fluxtube. The parameter  $R_2$  denotes the radial distance to the  $z$ -axis where the neutral density in the moon’s exosphere and hence, the Pedersen conductance, drop to zero. The parameters  $\gamma$  and  $\delta$  need to be determined such that  $\Sigma_P(r)$  is continuous at  $r = R_1$  and vanishes at  $r = R_2$ . We find

$$\gamma = \Sigma_A \exp(\delta R_2) \quad \text{and} \quad \delta = \frac{\ln\left(\frac{\Sigma_{P,0} + \Sigma_A}{\Sigma_A}\right) + \beta R_1}{R_2 - R_1}. \quad (8)$$

This result shows  $\delta > 0$ , that is, the modeled conductance profile does decay with distance  $r$  outside of the moon’s fluxtube and hence, has the anticipated shape of a “suspension bridge.”

We now calculate the radial component  $\Lambda_i(r)$  (where  $i = I, II, III$ ) of the potential  $\psi_i$  in the three coaxial cylinders defined by Equation 7. While in region (I), the analytical form of  $\Lambda_i(r)$  is given by Equation 6, the expression

$$\Lambda_{II}(r) = \frac{-K_3(\delta r + 1) + K_4 \exp(\delta r)}{r} \quad (9)$$

with constants  $K_3, K_4$  satisfies the potential equation in region (II). In region (III), the radial component of  $\psi_{III}$  can be expressed as

$$\Lambda_{III}(r) = E_0 r + \frac{K_5}{r} \quad (10)$$

with another constant of integration  $K_5$  (see, e.g., Saur et al., 2007 or Simon, 2015). The quantity  $E_0 = u_0 B_0$  denotes the magnitude of the undisturbed convective electric field.

The constants  $K_1, K_2, K_3, K_4$ , and  $K_5$  can be determined from the various boundary conditions of the potential problem. Since our setup does not include any delta-like singularity at the center  $r = 0$  of the conductance profile, the solution for  $\Lambda_i(r)$  needs to remain finite at that point. Applying de l’Hôpital’s rule to Equation 6 then yields  $K_1 = K_2$  and thus,

$$\Lambda_I(r) = K_1 \frac{\beta r - 1 + \exp(-\beta r)}{r}. \quad (11)$$

In addition, the potential  $\psi_i$  needs to be continuous at the boundaries between different regions, implying

$$\Lambda_I(r = R_1) = \Lambda_{II}(r = R_1) \quad \text{and} \quad \Lambda_{II}(r = R_2) = \Lambda_{III}(r = R_2). \quad (12)$$

At the transition between different regions, the potential also needs to satisfy boundary condition (A2) from the work of Saur et al. (1999). As shown by Simon (2015), for the case of a *continuous* conductance profile this condition reduces to

$$\left. \frac{d\Lambda_I(r)}{dr} \right|_{r=R_1} = \left. \frac{d\Lambda_{II}(r)}{dr} \right|_{r=R_1} \quad \text{and} \quad \left. \frac{d\Lambda_{II}(r)}{dr} \right|_{r=R_2} = \left. \frac{d\Lambda_{III}(r)}{dr} \right|_{r=R_2}, \quad (13)$$

that is, the radial component of the electric field is continuous across the interfaces between different cylinders. Thus, in contrast to the box-like conductance profiles used by, for example, Saur et al. (1999) or Simon, Saur, Kriegel, et al. (2011), or Simon, Saur, Neubauer, et al. (2011), the cylinder mantles  $r = R_1$  and  $r = R_2$  do *not* carry any surface charges.

Including the expressions for  $\Lambda_i(r)$  into the boundary conditions then yields a linear system of equations for the remaining four constants  $\underline{K} \equiv (K_1, K_3, K_4, K_5)$ ,

$$\underline{\xi} \cdot \underline{K} = \underline{c}, \quad (14)$$

where the constant matrix  $\underline{\xi}$  is given by

$$\underline{\xi} = \begin{pmatrix} \beta R_1 - 1 + \exp(-\beta R_1) & \delta R_1 + 1 & -\exp(\delta R_1) & 0 \\ 0 & -(\delta R_2 + 1) & \exp(\delta R_2) & -1 \\ 1 - (\beta R_1 + 1)\exp(-\beta R_1) & -1 & -(\delta R_1 - 1)\exp(\delta R_1) & 0 \\ 0 & 1 & (\delta R_2 - 1)\exp(\delta R_2) & 1 \end{pmatrix} \quad (15)$$

and the inhomogeneity vector reads  $\underline{c} = (0, E_0 R_2^2, 0, E_0 R_2^2)$ . This system can be solved for  $\underline{K}$ , for example, by using a computer algebra system. However, for the sake of brevity, we refrain from providing the lengthy expressions for the four constants here. The explicit expressions for these constants are *not* required to understand the ideas of the following derivations.

The solution for  $\psi_i(r, \phi) = \Lambda_i(r)\sin\phi$  (where  $i = I, II, III$ ) can now be applied to calculate various quantities of the Alfvénic interaction. As shown by Simon, Saur, Kriegel, et al. (2011); Simon, Saur, Neubauer, et al. (2011), the magnetic field  $\underline{B} = (B_x, B_y, B_z)$  near the Alfvén wings is given by

$$B_x = \frac{1}{\sqrt{M_A^2 + 1}} \left\{ \mp M_A \sqrt{B_0^2 - \mu_0^2 \Sigma_A^2} \left\{ \frac{1}{M_A^2 + 1} \left( \frac{\partial \psi_i}{\partial x} \right)^2 + \left( \frac{\partial \psi_i}{\partial y} \right)^2 \right\} \pm \mu_0 \Sigma_A \frac{\partial \psi_i}{\partial y} \right\} ; \quad (16)$$

$$B_y = \mp \frac{1}{\sqrt{M_A^2 + 1}} \mu_0 \Sigma_A \frac{\partial \psi_i}{\partial x} ; \quad (17)$$

$$B_z = \frac{1}{\sqrt{M_A^2 + 1}} \left\{ -\sqrt{B_0^2 - \mu_0^2 \Sigma_A^2} \left\{ \frac{1}{M_A^2 + 1} \left( \frac{\partial \psi_i}{\partial x} \right)^2 + \left( \frac{\partial \psi_i}{\partial y} \right)^2 \right\} - M_A \mu_0 \Sigma_A \frac{\partial \psi_i}{\partial y} \right\}. \quad (18)$$

In these expressions, the *upper* sign always refers to the *northern* wing, whereas the *lower* sign denotes the *southern* wing. One readily verifies the incompressible nature of the Alfvénic perturbations, that is,  $|\underline{B}| = B_0$ . The partial derivatives in Equations 16–18 can be calculated from our expressions for  $\Lambda_I(r)$ ,  $\Lambda_{II}(r)$ , and  $\Lambda_{III}(r)$  according to

$$\frac{\partial \psi_i}{\partial x} = \sin \phi \cos \phi \left\{ \frac{\partial \Lambda_i}{\partial r} - \frac{1}{r} \Lambda_i \right\} \quad \text{and} \quad \frac{\partial \psi_i}{\partial y} = \sin^2 \phi \left\{ \frac{\partial \Lambda_i}{\partial r} - \frac{1}{r} \Lambda_i \right\} + \frac{1}{r} \Lambda_i, \quad (19)$$

where again  $i = I, II, III$ . It is noted that neither of the two derivatives diverges along the symmetry axis  $r = 0$  of the conductance profile. We find

$$\lim_{r \rightarrow 0} \frac{\partial \psi_I}{\partial x} = K_1 \lim_{r \rightarrow 0} \left\{ \frac{2 - \beta r - (\beta r + 2) \exp(-\beta r)}{r^2} \right\} \sin \phi \cos \phi = 0 \quad (20)$$

and

$$\lim_{r \rightarrow 0} \frac{\partial \psi_I}{\partial y} = K_1 \lim_{r \rightarrow 0} \left\{ \frac{2 - \beta r - (\beta r + 2) \exp(-\beta r)}{r^2} \sin^2 \phi + \frac{\beta r - 1 + \exp(-\beta r)}{r^2} \right\} = K_1 \frac{\beta^2}{2}. \quad (21)$$

The potential  $\psi(x, y)$  can be used not only to calculate the magnetic field, but also the bulk velocity  $\underline{u}(x, y)$  of the deflected magnetospheric plasma. Using the constancy of the Elsässer variables  $\underline{Z}_{\mp}$  (see Equation 5 in Neubauer, 1980),

$$\underline{Z}_{\mp} \equiv \underline{u} \mp \frac{\underline{B}}{\sqrt{\mu_0 \rho_0}} = u_0 \mp \frac{B_0}{\sqrt{\mu_0 \rho_0}}, \quad (22)$$

we can solve for the flow field  $\underline{u}(x, y)$ :

$$\underline{u} = u_0 \pm \frac{B - B_0}{\sqrt{\mu_0 \rho_0}}. \quad (23)$$

In these expressions,  $\rho_0$  denotes the mass density of the (incompressible) magnetospheric plasma flow, whereas the upper and lower signs again refer to the northern and southern wings, respectively.

The solution for  $\psi(r, \phi)$  also determines the currents  $j_{\parallel}$  along the Alfvén wing characteristics. Without loss of generality, we restrict our discussion to the *southern* wing. In the northern wing, the sign of the wing-aligned currents would simply be reversed. According to Equation 9 of Neubauer (1980), these currents can be expressed as

$$j_{\parallel} = -\Sigma_A \Delta \psi. \quad (24)$$

In our setup we find

$$j_{\parallel, i} = -\Sigma_A \left\{ \frac{1}{r} \frac{\partial}{\partial r} \left( r \frac{\partial \Lambda_i}{\partial r} \right) - \frac{1}{r^2} \Lambda_i \right\} \sin \phi \quad (25)$$

for the respective region ( $i = I, II, III$ ) of the conductance profile. More specifically, this expression yields

$$j_{\parallel, I} = \Sigma_A K_1 \beta \frac{1 - (\beta r + 1) \exp(-\beta r)}{r^2} \sin \phi = \Sigma_A \beta \frac{\partial \Lambda_I}{\partial r} \sin \phi \quad (26)$$

for region *I* where the Pedersen conductance *increases* with distance  $r$  from the  $z$ -axis. In region *II* where  $\Sigma_P(r)$  gradually *decreases* to zero, we find

$$j_{\parallel, II} = -\Sigma_A \delta \frac{K_3 + K_4 (\delta r - 1) \exp(\delta r)}{r^2} \sin \phi = -\Sigma_A \delta \frac{\partial \Lambda_{II}}{\partial r} \sin \phi. \quad (27)$$

In agreement with, for example, Simon (2015) the currents along the wing characteristics vanish outside of the exosphere ( $r > R_2$ ), that is,  $j_{\parallel,II} \equiv 0$ . Making use of the continuity of  $\partial A_I / \partial r$  at the boundaries between adjacent cylinders, Equations 26 and 27 reveal that the currents along the wing characteristics are *discontinuous* at the interface of regions *I* and *II*, with the height of the jump given by

$$(j_{\parallel,I} - j_{\parallel,II}) \Big|_{r=R_1} = \Sigma_A (\beta + \delta) \frac{\partial A_I}{\partial r} \Big|_{r=R_1} \sin \phi. \quad (28)$$

The wing-aligned currents abruptly change their *direction* when moving from the ascending flank to the descending flank of the ionospheric conductance profile. While the magnetic field components are continuous across this boundary, the change in the direction of  $j_{\parallel}$  still generates a “spike” in the field. In addition, the wing-aligned currents are discontinuous at the outer edge of the ionospheric conductance profile. As can be seen from Equation 27,

$$j_{\parallel,II} \Big|_{r=R_2} \neq 0, \quad (29)$$

thereby generating another “spike” in the magnetic field. In other words, the changing sign of the slope of  $\Sigma_p(r)$  at the surface of the moon’s fluxtube as well as the “smooth” outer edge of the exosphere give rise to discontinuities in the wing-aligned currents and cause associated signatures in the magnetic field. Due to the translational invariance of the Alfvén wings along their characteristics, these signatures are observable even at large distances to the moon. This opens an avenue to constrain, for example, the extension of a moon’s gas envelope by using magnetic field observations from flybys through the distant Alfvén wings. Details will be discussed in Section 3.5.

### 2.3. What This Model Can Do

The model developed in Section 2.2 allows us to provide a completely analytical description of the Alfvénic plasma and field perturbations generated by the “suspension bridge”-like Pedersen conductance profile in a moon’s ionosphere. Since the incident magnetospheric flow conditions as well as the steepness and amplitude of the conductance profile are provided as input parameters for the calculations, this approach greatly facilitates the analysis of the fundamental physical processes that are driven by various key properties of the moon-magnetosphere system. In contrast to numerical models, extensive studies of the role that, for example, a certain upstream parameter plays in the interaction can be completed in a matter of minutes.

Most importantly, the model operates independent of artificial boundary conditions that are required in numerical models, and its output is not affected by, for example, too coarse grid resolution or an excess of numerical diffusion. In principle, the properties of the “pure” Alfvénic interaction can also be extracted from a numerical model, provided that the simulation domain encompasses a sufficiently large region around the moon. Since the Alfvén wings are discernible only at large distances where the contribution of ionospheric currents to the magnetic field has disappeared, this would require a simulation box with a size of tens of moon radii, often at the expense of adequate grid resolution in the vicinity of the obstacle itself. Besides, the ability of such a numerical approach to resolve, for example, any magnetic discontinuities at the surface of the moon’s fluxtube would still be limited by the grid resolution and numerical diffusion. This represents a significant challenge for numerical simulations of, for example, the surface currents generated by Enceladus’ magnetospheric interaction (Kriegel et al., 2014; Saur et al., 2007; Simon et al., 2014).

### 2.4. What This Model Can Not Do

The analytical model captures only the Alfvénic (incompressible) component of a moon’s magnetospheric interaction. In isolation, the associated plasma and field perturbations can be observed only in the “Alfvénic far field,” that is, at a distance of several moon radii where the contributions of transverse currents in the obstacle’s ionosphere have faded away (Neubauer, 1980). In the immediate vicinity of the moon, the wing-aligned currents couple to ionospheric Pedersen and Hall currents (Neubauer, 1998; Saur et al., 1999;

Simon, Saur, Kriegel, et al., 2011; Simon, Saur, Neubauer, et al., 2011) which generate additional (compressional) perturbations in flow quantities and magnetic field. Examples of such “local” contributions to the interaction are the formation of a magnetic pile-up region at the obstacle’s ramside and the associated magnetic rarefaction region in its downstream hemisphere (e.g., Arnold et al., 2020). While the piled-up field lines may locally enhance the deflection of incident magnetospheric particles around the moon (e.g., Paranicas et al., 2000), this effect cannot be captured within the framework of an analytical treatment.

Also, there is so far no analytical solution available for the incompressible, non-linear fluid equations that explicitly takes into account the modification of the Alfvénic perturbations by a (permanent or induced) dipole field from the moon’s conducting interior. In the Alfvénic far field, such a dipole mainly causes a reduction in the cross-sections of the Alfvénic fluxtubes and a slight displacement of their locations with respect to the moon, compared to the case of a “purely” ionospheric obstacle (Neubauer, 1999; Volwerk et al., 2007). In principle, the shrinkage of the Alfvén wing tubes can be taken into account by reducing the radii  $R_1$  and  $R_2$  of the region occupied by the obstacle. However, there is so far no simple method available to express the Alfvén wing perturbations in terms of, for example, a moon’s induced magnetic moment. This limits the applicability of the analytical approach to Ganymede which possesses a strong, permanent dipole moment of its own. The induced magnetic moments observed at, for example, Callisto and Europa are time-varying (Kivelson et al., 1999; Zimmer et al., 2000) and average out when considering a full synodic rotation. For these two moons, the analytical model is highly suitable to describe the Alfvénic interaction for the “average” state of the system. This state is well represented by the induced magnetic moment being zero and the moon being located at the center of the Jovian plasma sheet where the ambient magnetospheric field points approximately southward (e.g., Kivelson et al., 1999, 2009), as assumed by our approach. Considering the average state of the moon-magnetosphere interaction is helpful when analyzing physical processes that take place on time scales of many synodic rotations, such as the erosion of the moon’s surface by incident magnetospheric particles (e.g., Cassidy et al., 2013).

The restriction of the analytical approach to axisymmetric ionospheric conductance profiles precludes the incorporation of ram-wake or day-night asymmetries in a moon’s neutral gas envelope, as identified at, for example, Europa (Arnold et al., 2019; Plainaki et al., 2013; Rubin et al., 2015) or Callisto (Hartkorn et al., 2017; Liuzzo et al., 2015). While the condition  $M_A \ll 1$  is well fulfilled at the inner Galilean moons of Jupiter (Kivelson et al., 2004) and many icy moons of Saturn (Simon et al., 2015), Callisto and Titan were found to be exposed to a *super*-Alfvénic magnetospheric plasma along at least part of their orbits (Arridge et al., 2011; Kivelson et al., 2004; Simon et al., 2015). In such a scenario, the notion of the perturbations in the flow pattern and magnetic field components being weak compared to the upstream values is no longer applicable.

Our analytical model cannot capture the dynamics of magnetospheric particles with energies in the keV-MeV regime, which are mostly governed by their large gyroradii (see, e.g., Paranicas et al., 2009). However, the electromagnetic fields obtained from our approach can be incorporated into tracing simulations that track the motion of these particles through a moon’s perturbed magnetospheric environment (e.g., Breer et al., 2019; Liuzzo et al., 2019a, 2019b). In particular, including the analytical representations for the fields in such a tracing model can provide an initial idea of how energetic particle dynamics are changed compared to motion through uniform fields.

### 3. Case Study: Europa’s Magnetospheric Interaction

In this section, we explore how the “suspension bridge”-like Pedersen conductance profile  $\Sigma_p(r)$  of a moon’s ionosphere maps into the Alfvén wings. We note that detailed comparisons of the (magnetic) interaction signatures obtained for a “suspension bridge”-like conductance profile and earlier, box-like representations of the model ionosphere are given by Simon (2015). Since the conductance profile applied in that preceding study is qualitatively similar to the one employed here, we refrain from providing another detailed comparison to results from earlier iterations of the model. Instead, we focus on novel physical aspects of the interaction which have not yet been analyzed in preceding publications.

### 3.1. Model Parameters

As an example, we analyze the interaction between Europa (radius  $R_E = R_1 = 1,560.8$  km) and its magnetospheric plasma environment. The upstream parameters chosen for our model setup are representative of the center of Jupiter's magnetospheric plasma sheet and have been adopted from Arnold et al. (2020) and Blöcker et al. (2016). The thermal magnetospheric ion population is assumed to consist of one singly charged species of mass  $m = 18.5$  amu and number density  $n_0 = 60 \text{ cm}^{-3}$ , overtaking Europa at a relative velocity of  $\underline{u}_0 = (100 \text{ km/s}, 0, 0)$ . In combination with a magnetospheric background field of  $\underline{B}_0 = (0, 0, -450 \text{ nT})$ , these values yield an Alfvén conductance of  $\Sigma_A = 2.6$  S and an Alfvénic Mach number of  $M_A = 0.34$ . Thus, the Alfvén wing characteristics are inclined against the north-south direction by only about  $\arctan M_A = 18.7^\circ$ , which is well within the realm of applicability of our model. We note that there is no consensus in the literature on the upstream plasma moments near Europa at a given distance to the center of the Jovian plasma sheet (see, e.g., Bagenal & Delamere, 2011; Kurth et al., 2001; Roth, Retherford, et al., 2014). However, there is agreement on the facts that the upstream flow is clearly sub-Alfvénic and that thermal ion gyroradii are sufficiently small to capture numerous key features of the interaction within the framework of a fluid approach (e.g., Kivelson et al., 2009). Choosing a different set of upstream conditions would only slightly change the magnitudes and extensions of the modeled perturbation signatures near Europa, but would not affect our general conclusions on the involved physics. The set of parameters chosen here was found suitable to best visualize the underlying physical processes. We emphasize that the purpose of our investigation is *not* to explain/reproduce a specific set of spacecraft observations (although the model can certainly be applied in such a way).

Very little information on the Pedersen and Hall conductances of Europa's ionosphere can be found in the literature: Kivelson et al. (2004) and Saur et al. (2013) give a typical value of  $\Sigma_P \approx 30$  S for the Pedersen conductance, while the Hall conductance  $\Sigma_H$  is suggested to be about a factor of 3 smaller. Taking a look at Equation 7, we set the “baseline” conductance to  $\Sigma_{P,0} = 3$  S and choose a value of  $\beta = 1/(3H)$  for the steepness of the conductance profile within the Europa fluxtube. The parameter  $H$  denotes the scale height of Europa's neutral gas envelope. We assume a value of  $H = 100$  km, consistent with the models of Arnold et al. (2019, 2020) and Blöcker et al. (2016). In agreement with Blöcker et al. (2016) and Saur et al. (1998, 2013), the ionospheric Pedersen conductance is set to disappear at a distance of  $R_2 = R_E + 5H \approx 1.32R_E$  to the  $z$ -axis. Under these conditions, the average Pedersen conductance,

$$\langle \Sigma_P(r) \rangle = \frac{1}{R_2} \int_{r=0}^{r=R_2} \Sigma_P(r) dr, \quad (30)$$

has a value of  $\langle \Sigma_P(r) \rangle \approx 185$  S, which is larger, but still of the same order of magnitude as the value proposed by Kivelson et al. (2004). While the resulting sub-Alfvénic interaction may be slightly stronger than in reality, the chosen parameters were found to facilitate the identification of characteristic signatures in, for example, the magnetic field and the energy flux pattern at the edges of the Europa fluxtube. We also note that  $\langle \Sigma_P \rangle \gg \Sigma_A$  is fulfilled for either choice of  $\langle \Sigma_P \rangle$ , let it be 30 S or 185 S. Therefore, the *interaction strength*

$$\alpha \equiv \frac{\langle \Sigma_P \rangle}{\langle \Sigma_P \rangle + 2\Sigma_A}, \quad (31)$$

which (roughly) measures the electric field reduction within the Alfvénic fluxtubes and the associated “intensity” of the flow deflection (see Equation A7 in Saur et al., 1999 and Equation 17 in Saur et al., 2013), differs by only 12% between the two choices of the average Pedersen conductance: For  $\langle \Sigma_P \rangle = 30$  S, we find  $\alpha \approx 85\%$ , whereas our choice of  $\langle \Sigma_P \rangle \approx 185$  S yields an interaction strength of  $\alpha \approx 97\%$ .

The obstacle that Europa's ionosphere represents to the incident magnetospheric plasma consists mainly of the steep outer flank of the conductance profile outside of the Europa fluxtube ( $r > R_2$ ) that is initially encountered by the impinging plasma. Using Equation 8, the parameters  $\Sigma_{P,0}$ ,  $\beta$ , and  $R_2$  chosen in our model setup yield a value of  $\tilde{H} = 1/\delta \approx 84$  km for the scale length of this exponential decay. The exponential shape of the conductance profile and the value of  $\tilde{H}$  are consistent with Galileo observations of Europa's environment: As demonstrated by Blöcker et al. (2016), an exponential decrease of the ionospheric con-

ductance outside of the Europa fluxtube is required to explain the steep gradient seen in the magnetic field during the Galileo E17 flyby. These authors also showed that the scale length  $\tilde{H}$  can be expressed as

$$\frac{1}{\delta} = \tilde{H} = \frac{HH_i}{H + H_i}, \quad (32)$$

where  $H$  denotes the scale height of Europa's neutral gas envelope and  $H_i$  represents the scale height of the moon's ionosphere. Values for the neutral scale height, as documented in the literature, are in the range of  $H = 100\text{--}150$  km (e.g., Arnold et al., 2019; Blöcker et al., 2016; Saur et al. 1998). Based on six radio occultation observations during the Galileo mission, Kliore et al. (1997) determined a range of  $H_i = (240 \pm 40)$  km for Europa's ionospheric scale height. Hence, possible values for  $\tilde{H}$  range from 67 km up to 98 km, which is consistent with the choice of this parameter in our model. Our value of  $\tilde{H} \approx 84$  km is located approximately in the middle of the range of "allowed" decay scales.

In other words, our assumed values for both, the radial extension of the ionospheric Pedersen conductance profile ( $r = R_2$ ) and the length scale  $\tilde{H} = 1 / \delta$  of the exponential decay outside of the Europa fluxtube are in agreement with actual observations. Having reconciled all free parameters of the conductance profile in region III ( $\gamma$  and  $\delta$ , see Equations 7 and 8) with observations, this also implies that the modeled "amplitude" of the conductance peak at  $r = R_1$  is consistent with available data (although there are currently no direct observations available of the Pedersen conductance at the edge of the Europa fluxtube). Our choice of the free parameters in region I simultaneously allows to include an average Pedersen conductance  $\langle \Sigma_P(r) \rangle$  of the same order of magnitude as estimated by Kivelson et al. (2004). Thus, although no comprehensive model of Europa's ionospheric Pedersen conductance profile is currently available in the literature, our approach is "anchored" as much as possible into observations from multiple Galileo instruments and results from several preceding modeling studies. It is therefore very reasonable to consider the results of the following sections to be quantitatively relevant for the actual plasma interaction scenario at Europa.

We also note that at Europa, the ionospheric Hall effect would not significantly alter our modeled magnetic signatures and the deflection pattern of the magnetospheric flow. Assuming a "worst-case scenario," that is, a Hall conductance of  $\langle \Sigma_H \rangle = 10$  S and a Pedersen conductance of *only*  $\langle \Sigma_P \rangle = 30$  S (Kivelson et al., 2004), we find that the electric field  $\underline{E}$  within the Alfvénic fluxtube would be rotated by an angle of only

$$\Theta = \arctan \left\{ \frac{\langle \Sigma_H \rangle}{\langle \Sigma_P \rangle + 2\Sigma_A} \right\} \approx 15.9^\circ \quad (33)$$

against its direction ( $-\underline{e}_y$ ) *without* the ionospheric Hall effect included (using Equation A11 from Saur et al., 1999). However, the Hall effect may play a much more important role in the vicinity of local atmospheric inhomogeneities (plumes), as discussed by Arnold et al. (2019) and Blöcker et al. (2016).

The conductance profile  $\Sigma_P(r)$  resulting from these parameters is displayed in Figure 1. The profile is rotationally symmetric around the  $z$ -axis. Thus, for a cut along, for example, the  $x$ - or the  $y$ -axis, the profile has the shape of a suspension bridge (one half of which is shown in Figure 1). In three dimensions, the ionospheric conductance profile has the shape of a bowl or a basin. The value of  $\Sigma_P(r)$  peaks at the surface  $r = R_E$  of the Europa fluxtube where the magnetospheric field lines no longer thread the solid body of the moon.

### 3.2. Model Validation: Electrostatic Potential and Flow Deflection

To demonstrate that the analytical model produces adequate results, Figure 2 displays the isolines of the electrostatic potential  $\psi(x, y)$  in an arbitrary plane perpendicular to the  $z$ -axis. Due to the frozen-flux theorem  $\nabla \psi = \underline{u} \times \underline{B}$  and the assumed two-dimensionality of the problem, these isolines coincide with the streamlines of the flow field  $\underline{u}(x, y)$ . At large distances to Europa,  $\psi(x, y)$  is identical to the potential  $\psi_0 = E_0 y$  of the unperturbed convective electric field, that is, the isolines (and flow contours) are parallel to the  $x$ -axis. However, in the vicinity of the moon, the flow field is strongly deflected around the obstacle, with the deflection pattern being symmetric between the Jupiter-facing ( $y > 0$ ) and Jupiter-averted ( $y < 0$ ) hemispheres. The spike in the ionospheric conductance profile at the surface of the Europa fluxtube provides efficient

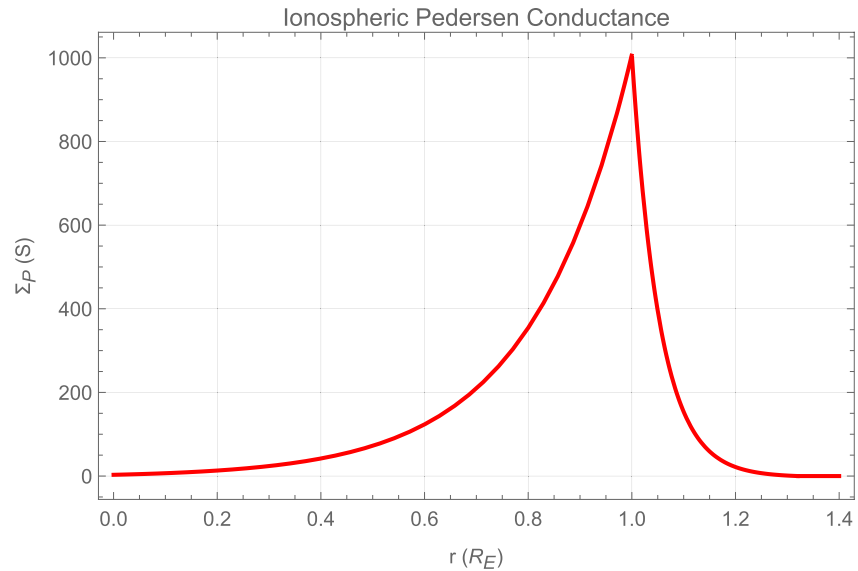


**Figure 1.** Pedersen conductance profile of Europa's ionosphere in our model setup. The figure illustrates how  $\Sigma_P(r)$  changes as a function of distance  $r = \sqrt{x^2 + y^2}$  to the  $z$ -axis. The model parameters have been chosen as detailed in Section 3.1.

shielding against the incident magnetospheric flow: Most of the isolines shown here are bent around the “core region”  $r = R_2$  of the Alfvén wing. From the set of isolines selected in Figure 2, only the one along the  $x$ -axis does not alter its direction. However, the flow along the  $x$ -axis is strongly decelerated to velocities below 10 km/s by the Alfvénic interaction (plot not shown here). The strong deflection of the magnetospheric plasma around Europa is consistent with the large value of the interaction strength at the center of Jupiter's magnetospheric plasma sheet ( $\alpha \approx 97\%$ ), suggesting that only about 3% of the “incoming” streamlines may still intersect the obstacle.

Taking a more quantitative look at the flow velocity, Figure 3 shows the components  $u_x$  and  $u_y$  along two cuts parallel to the  $x$ -axis in the Jupiter-facing (Figure 3a) and Jupiter-averted (Figure 3b) hemispheres. The  $u_x$  profile (red) is identical in both cases: The flow is decelerated at the upstream flank of the Alfvén wing ( $x < -R_2$ ), then accelerates as it passes the obstacle ( $-R_2 \leq x \leq +R_2$ ) and reduces its speed again at the downstream side ( $x > R_2$ ). The  $u_y$  component (blue) is exactly antisymmetric between the ( $y < 0$ ) and ( $y > 0$ ) hemispheres, corresponding to a deflection away from Europa at the upstream side of the wing and a subsequent deflection toward the moon at its downstream side. The turning point between both directions of  $u_y$  is located at  $x = 0$  where the flow field is parallel to the  $x$ -axis. This behavior is also consistent with the shape of the isolines shown in Figure 2, demonstrating that the modeled flow field fully reproduces the expected features of the sub-Alfvénic interaction under the assumption of  $\Sigma_H \equiv 0$ . For two-dimensional visualizations of the magnetic field components, the reader is referred to Figure 8 of Simon, Saur, Kriegel, et al. (2011). Although based on a piecewise constant conductance profile, many properties of the magnetic field patterns described in that preceding study are still qualitatively consistent with the output of our expanded model.

### 3.3. Number Flux of Magnetospheric Plasma

The precipitation of magnetospheric ions and electrons onto Europa constitutes a critical agent in weathering its surface and releasing particles into its space environment (sputtering), ultimately contributing to the moon's exosphere and the neutral gas torus along its orbit (e.g., Cassidy et al., 2013; Dalton et al., 2013; Johnson et al., 2009 and references therein). Numerous models attempting to constrain the spatial distribution of the magnetospheric charged particle flux onto Europa's surface treat the ambient electromagnetic fields as uniform, that is, they take into account neither any induced magnetic field from the moon's interior nor the perturbations generated by the interaction with the incident magnetospheric plasma (e.g., Cassidy et al., 2013; Plainaki et al., 2013; Pospieszalska & Johnson, 1989). However, in recent years several

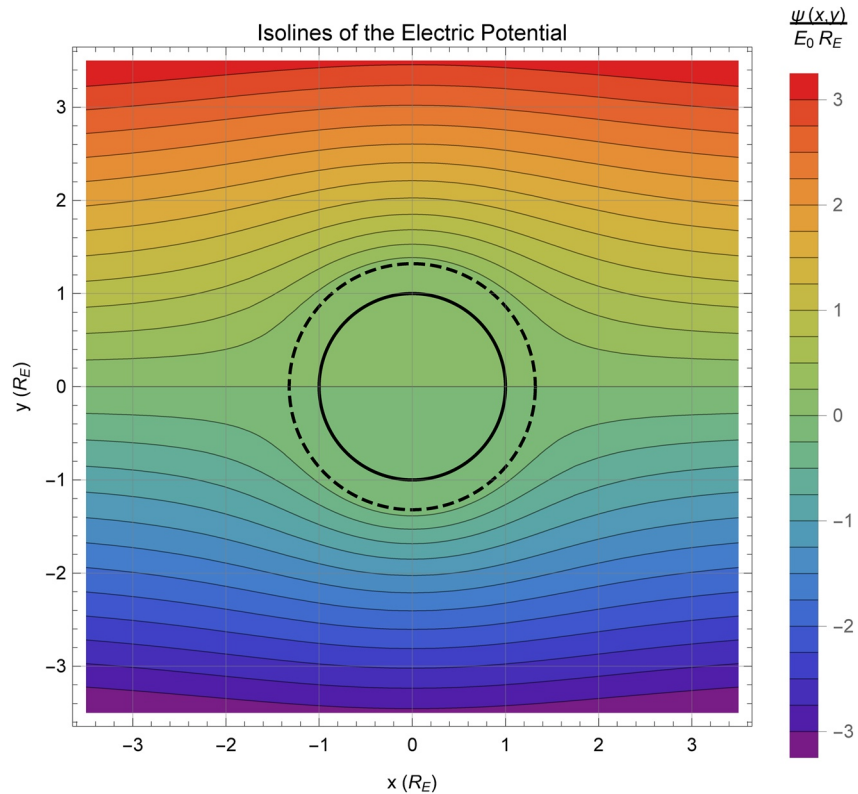


**Figure 2.** Isolines of the electrostatic potential  $\psi(x, y)$  in an arbitrary plane  $z = \text{const}$  perpendicular to the Alfvén wing characteristics. The values of  $\psi$  have been normalized to the potential  $E_0 R_E$  of the unperturbed convective electric field  $\underline{E}_0 = -\underline{u}_0 \times \underline{B}_0$  at Europa’s Jupiter-facing apex ( $x = 0, y = +1R_E, z = 0$ ). The solid black circle (radius  $r = R_1 = R_E$ ) denotes the projection of Europa onto the cutting plane, whereas the dashed black circle (radius  $r = R_2$ ) denotes the outer boundary of the moon’s exosphere in our model. In contrast to preceding model formulations that take into account the ionospheric Hall effect (see, e.g., Figure 3 in Saur et al., 2007) the deflection pattern is precisely symmetric between the Jupiter-facing ( $y > 0$ ) and Jupiter-averted ( $y < 0$ ) hemispheres.

modeling studies have revealed that the electromagnetic field perturbations generated by an icy moon’s magnetospheric interaction drastically alter the precipitation pattern of charged particles onto its surface, compared to uniform fields (e.g., Breer et al., 2019; Liuzzo et al., 2019a, 2019b; Rubin et al., 2015). Not only do these field perturbations partially shield the entire surface from charged particle irradiation, but they can even generate “islands” of nearly zero magnetospheric ion flux that remain protected on time scales of an entire orbit. A prominent example was recently described by Arnold et al. (2020) and Breer et al. (2019): The plumes of water vapor that sporadically emerge from Europa’s surface (e.g., Roth, Saur, et al., 2014) locally generate a “bulge” in the magnetic field that deflects impinging magnetospheric ions away from the plume’s source region on the surface. In other words, the field perturbations associated with a plume may shield any potential biomatter that has “rained down” onto Europa’s surface from alteration by precipitating magnetospheric ions, at least as long as the source is active.

The magnetospheric plasma incident upon Europa contains ions with energies around or below  $E = 1$  keV (referred to as the “thermal” plasma) as well as an energetic component with  $E$  ranging from a few keV up to several hundreds of MeV (e.g., Cooper et al., 2001; Paranicas et al., 2000). The interaction between the thermal plasma and the moon’s exosphere is the root cause of magnetic field pile-up, draping and the purely Alfvénic field perturbations observable at larger distances (e.g., Arnold et al., 2020; Blöcker et al., 2016). Many aspects of thermal ion dynamics near Europa can be captured within the framework of a continuum picture (e.g., Blöcker et al., 2016; Rubin et al., 2015; Schilling et al., 2008). The energetic ion population is so dilute that its dynamics can be treated in the test particle regime (e.g., Breer et al., 2019; Mauk et al., 2004). However, the gyroradii of the energetic ions are generally so large that individual (macro)

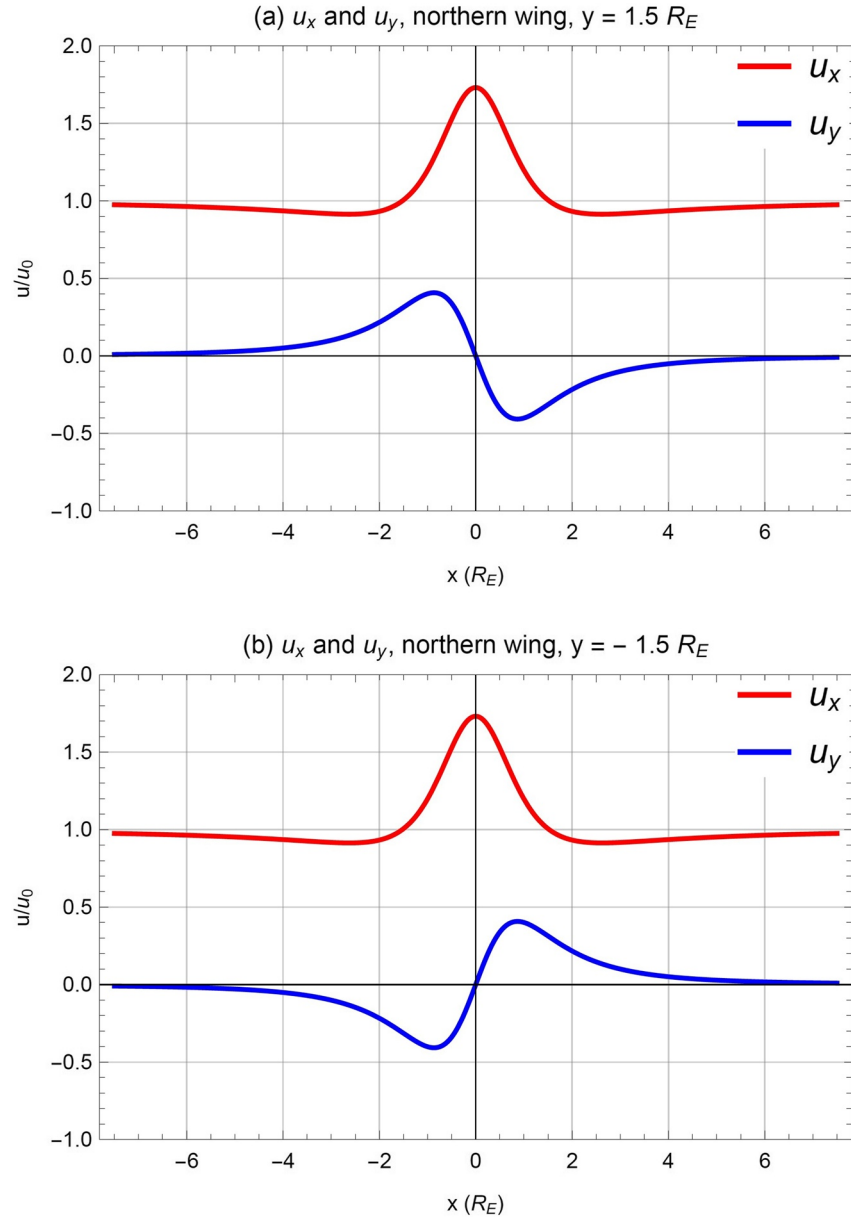


**Figure 3.** Components of the bulk velocity  $u(x, y)$  of the magnetospheric plasma along the (a)  $y = +1.5R_E$  and (b)  $y = -1.5R_E$  lines in an arbitrary plane  $z = \text{const}$  perpendicular to the northern Alfvén wing characteristic. Both cuts are located slightly outside of Europa’s exosphere which “ends” at  $y = \pm R_2 \approx \pm 1.32R_E$ . The components of  $u$  have been normalized to the bulk velocity  $u_0 = 100$  km/s of the undisturbed magnetospheric upstream flow. The flow patterns in the vicinity of the southern wing are identical to the ones displayed here.

particles need to be traced in order to determine their contribution to surface irradiation (Breer et al., 2019; Cassidy et al., 2013). In this section, we therefore focus on constraining the role of the moon-magnetosphere interaction in altering the *thermal* ion flux pattern onto Europa, compared to uniform fields.

As discussed in Section 2.4, the purely Alfvénic perturbations are discernible only at sufficiently large distances from Europa where the local contributions of Pedersen and Hall currents to field pile-up and draping have vanished. Resolving the dynamics of magnetospheric ions in the complex field geometry near Europa requires the application of numerical models. However, only very recently have the field perturbations been acknowledged as a key component in determining surface irradiation patterns (Breer et al., 2019). To better understand the underlying physical processes, it is therefore also relevant to constrain the contribution of

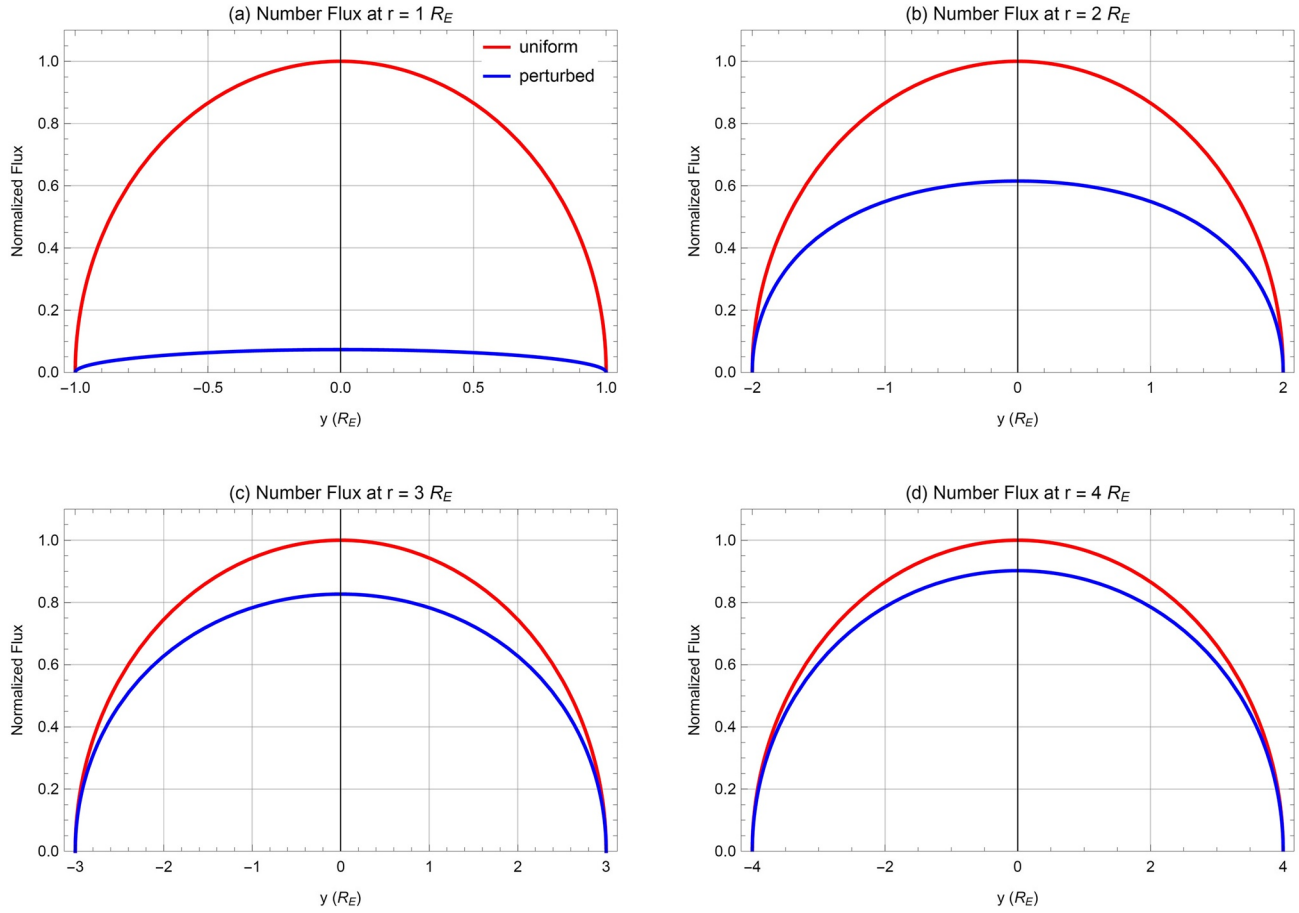


**Figure 4.** Number flux of the thermal magnetospheric plasma onto the ramside ( $x < 0$ ) of a system of coaxial cylinders, centered around the  $z$ -axis and located at (a) Europa’s surface  $r = 1R_E$ , (b)  $r = 2R_E$ , (c)  $r = 3R_E$ , and (d)  $r = 4R_E$ . The “perturbed” fluxes, taking into account flow deflection around the Alfvén wings, are displayed in blue. In each panel, the red line illustrates the number flux that would be deposited by the uniform magnetospheric upstream flow. All quantities displayed are normalized to  $n_0u_0$ . Please note that the different radii of the cylinders lead to different ranges of the (horizontal)  $y$ -axis in each panel. Since the magnetospheric field is exactly perpendicular to the upstream flow direction and thermal ion gyroradii (about 40 km) are negligible compared to the size of Europa, the precipitation pattern is perfectly symmetric between the moon’s Jupiter-facing and Jupiter-averted hemispheres.

the Alfvénic perturbations *in isolation* to the deflection of (thermal) magnetospheric ions away from Europa’s surface. The analytical model developed in Section 2.2 is highly suitable for this task. Here, we study the depletion of the *number* flux of thermal magnetospheric plasma onto the surface, while Section 3.4 deals with the flux of kinetic energy carried by the flow.

To illustrate the attenuation of the thermal plasma’s number flux with distance to the surface, Figure 4 displays (in blue) the flux

$$\mathcal{F} \equiv n_0 |\underline{u} \cdot \underline{e}_r| = n_0 |u_x(x, y) \cos \phi + u_y(x, y) \sin \phi| \quad (34)$$

through the ramside surfaces of a system of coaxial cylinders, located at  $r = 1R_E, 2R_E, 3R_E, 4R_E$ . In Equation 34,  $u_x$  and  $u_y$  denote the components of the bulk velocity  $\underline{u}$  at the respective location. For reference, we also show (in red) the “baseline” flux

$$\mathcal{F}_0 \equiv n_0 u_0 |\cos \phi| \quad (35)$$

that would be deposited by the undisturbed upstream flow (moving at velocity  $u_0 \underline{e}_x$ ) onto the respective location. As pointed out by Cassidy et al. (2013), the unperturbed flux of thermal magnetospheric ions onto Europa’s surface forms a “bullseye” pattern around the ramside apex, that is, the flux peaks at point

( $x = -1R_E, y = z = 0$ ), then weakens in all surface directions with rotational symmetry around the  $x$ -axis, and ultimately disappears downstream of the  $x = 0$  plane. Since our Alfvén wing model exhibits translational invariance along the  $\pm z$  directions, we can capture only the *longitudinal* decrease in flux (as expressed through the angle  $\phi$ , see Equation 35).

As can be seen from Figure 4a, flow deflection by the Alfvén wings alone reduces the thermal number flux reaching the innermost cylinder by more than an entire order of magnitude, compared to a scenario that treats the fields as uniform. Flow deflection already commences as far as  $4R_E$  upstream of Europa (see Figure 4d), and the flux toward the surface is reduced by either completely diverting the plasma mass elements out of the moon’s “path” or by increasing the inclination of their velocity vectors with respect to the surface. The number flux that is still able to reach a certain distance to Europa drops monotonically, but non-linearly with distance  $r$ . Most importantly, however, deflection of the flow by the Alfvén wings alone retains the overall shape of the “bullseye”-like precipitation pattern given by Equation 35. As can be seen from Figure 4, at any given distance to the moon, the flux still reaches its maximum at  $y = 0$  and then decreases symmetrically toward both edges of the respective cylinder mantle. Thus, while the Alfvén wings clearly weaken the flow of impinging plasma, maximum deposition of matter still occurs around Europa’s ramside apex. As we will see in Section 3.4, the situation is drastically different for the spatial distribution of the *energy* flux.

Any additional complexities in the surface precipitation patterns are generated by compressional components of the interaction due to Pedersen and Hall currents in Europa’s ionosphere. However, a recent study by Addison et al. (2021) investigated in detail the role of Europa’s magnetic pile-up region in protecting the moon’s ramside surface from precipitating thermal ions. By combining the electromagnetic fields from a hybrid model with a particle tracing tool, these authors demonstrated that the magnetic gradient drift experienced by a thermal oxygen ion within the pile-up region will deflect its guiding center trajectory by less than  $0.07^\circ$ . Even for ions in the MeV regime (which are *not* captured by our model), the deflection angle was still found to be way below  $10^\circ$ . Besides, in full quantitative agreement with our results, the (more complex) model of Addison et al. (2021) determined the thermal magnetospheric ion flux onto Europa’s surface to be about 1–2 orders of magnitude weaker than the upstream flux. Thus, while the Alfvén wings generate a protective “envelope” around Europa that partially shields the surface from the impinging plasma, the additional protection rendered by ramside field pile-up was shown to be far weaker than hypothesized by preceding studies (e.g., Paranicas et al., 2000). Therefore, the findings of Addison et al. (2021) imply that the results presented in this section can be considered a very reasonable approximation to emulate ion precipitation onto Europa at equatorial latitudes.

We again emphasize that the conclusions in this section hold only as long as the dynamics of the incident ions can be described in the fluid picture. At energies of a few 10s of keV, ion gyroradii (especially of heavy magnetospheric species like oxygen and sulfur) become so large that the particles can partially avoid impacting Europa by gyrating around it (Breer et al., 2019; Cassidy et al., 2013; Paranicas et al., 2009).

### 3.4. Energy Deposition by Magnetospheric Ions

The energy flux deposited by the incident magnetospheric plasma may affect a moon’s neutral gas envelope as well as its surface. The energy carried by the flow into the exosphere can lead to ionization of neutrals (e.g., Regoli et al., 2016), thereby contributing to the generation of the ionosphere which, in turn, constitutes the major obstacle to the plasma. Besides, to understand surface weathering at Europa, the discrimination between the *number* flux  $\mathcal{F}$  and the *energy* flux  $\mathcal{E}$  of the magnetospheric flow may become important. For instance, Dalton et al. (2013) searched for a correlation between the charged particle influx pattern and observed variations in the concentration of sulfuric acid ( $\text{H}_2\text{SO}_4$ ) deposits across the moon’s surface. These authors suggested that both, the *number* flux of magnetospheric sulfur ions and the *energy* flux of impinging energetic electrons are enhanced in regions where the  $\text{H}_2\text{SO}_4$  concentration is high. Dalton et al. (2013) proposed that the kinetic energy deposited by magnetospheric electrons “softens” the surface materials, thereby facilitating the implantation of sulfur ions and leading to the generation of  $\text{H}_2\text{SO}_4$ .

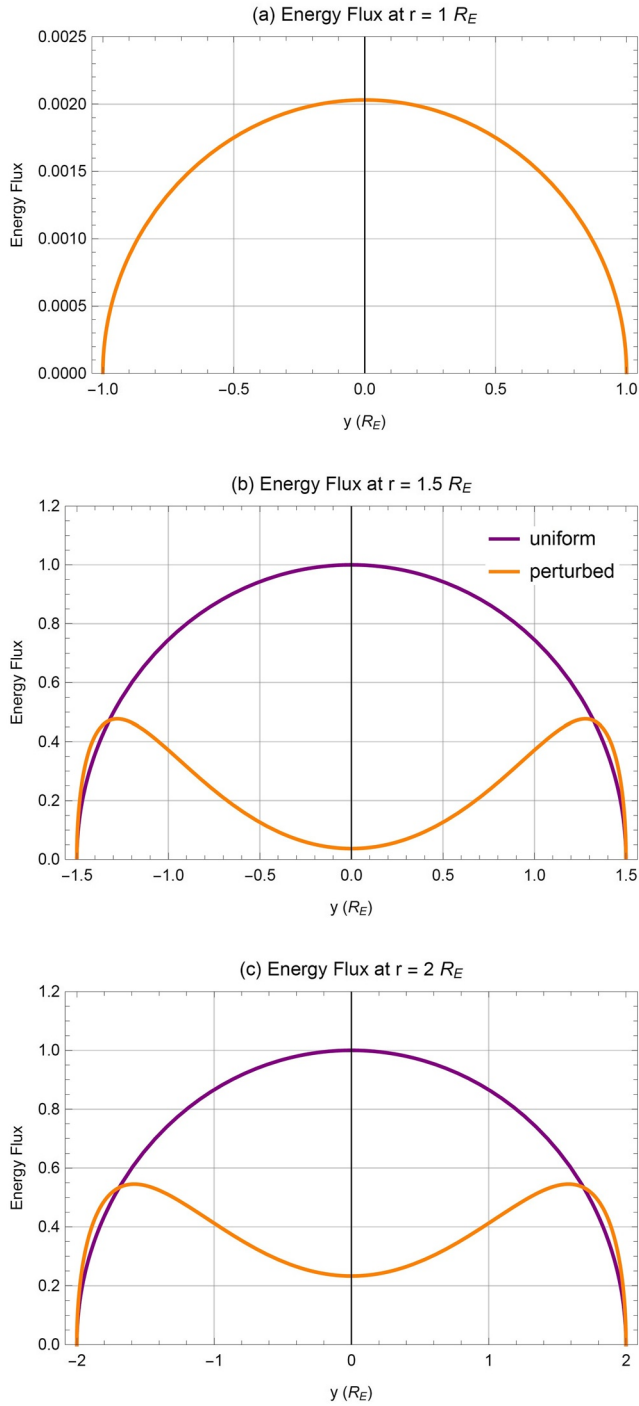


**Figure 5.** Energy flux deposited by the thermal magnetospheric plasma onto the ramside surfaces of three coaxial cylinders, located at (a) the surface of Europa  $r = 1R_E$ , (b)  $r = 1.5R_E$ , and (c)  $r = 2R_E$ . The orange lines display the energy flux of the deflected magnetospheric plasma, whereas the purple lines provide the energy flux carried by the undisturbed flow for reference. All quantities shown in the figure are normalized to the upstream energy flux  $n_0 m u_0^3 / 2$ . Please note that the vertical axis in panel (a) covers a much narrower flux range than in panels (b) and (c). Therefore, the “baseline” energy flux of the unperturbed flow cannot be included in panel (a). Also, the different radii of the three cylinders again lead to different ranges of the  $y$  axes in the individual panels.

Understanding the detailed physics of these processes requires to study charged particle precipitation across the entire energy range (from eV to MeV) observed near Europa’s orbit. This could be done by, for example, carrying out tracing simulations similar to those of Breer et al. (2019). However, our analytical model allows to gain first insights into the effect of Europa’s Alfvénic interaction on the distribution of the kinetic energy flux deposited by the thermal (corotating) magnetospheric flow. For this purpose, Figure 5 displays (in orange) the kinetic energy flux

$$\mathcal{E} \equiv \frac{1}{2} n_0 m \underline{u}^2 \left| \underline{u} \cdot \underline{e}_r \right| = \frac{1}{2} n_0 m \underline{u}^2 \left| u_x(x, y) \cos \phi + u_y(x, y) \sin \phi \right| \quad (36)$$

carried by the flow (see Saur et al., 2013) onto the ramside surfaces of a system of coaxial cylinders located at  $r = 1R_E, 1.5R_E, 2R_E$ . Due to the dependency of  $\mathcal{E}$  on the third power of the velocity  $|\underline{u}|$ , the changes in the energy flux pattern with distance evolve more drastically than in the number flux. Therefore, we have decided to “zoom in” and choose a set of reference cylinders closer to the surface than in Figure 4. For comparison, Figure 5 also displays (in purple) the kinetic energy flux carried by the undisturbed magnetospheric flow

$$\mathcal{E}_0 \equiv \frac{1}{2} n_0 m \underline{u}_0^2 \left| u_0 \cos \phi \right| \quad (37)$$

toward the surface.

As illustrated in Figures 5b and 5c, as long as the cylinder is located above the top of Europa’s exosphere (which “ends” at  $R_2 \approx 1.32R_E$ ), the depletion of the energy flux when approaching the moon looks drastically different from that of the number flux (see Figure 4). The energy flux experiences the strongest drop along the  $x$ -axis, that is, directly upstream of the moon’s ramside apex. At the Jupiter-facing and Jupiter-averted flanks of the interaction region, the flow is accelerated around the obstacle, thereby enhancing the energy flux compared to the ramside apex and producing two prominent maxima in the energy flux at the “edges” of the cylinders. In other words, at sufficiently large distance from the moon’s surface, the number and kinetic energy fluxes deposited by the magnetospheric flow do *not* peak at the same location.

However, once the flow has entered the densest regions of the moon’s ionosphere (see Figure 5a), its bulk velocity  $\underline{u}$  again becomes more aligned with the  $x$ -axis (although the magnitude  $|\underline{u}|$  is drastically reduced, compared to upstream). As shown by, for example, Simon, Saur, Kriegel, et al. (2011) and Simon, Saur, Neubauer, et al. (2011), the magnetic field perturbations outside of the Alfvénic fluxtubes exhibit a dipolar shape in planes perpendicular to the wing characteristics. However, inside the Alfvén wings these perturbations are aligned with the  $x$ -axis (see Figure 8 in that work). According to Equation 23, the perturbation pattern of the magnetic field then maps into the flow velocity as well. Therefore, the kinetic energy flux deposited at  $r = 1R_E$  exhibits a similar pattern as the number flux: The maximum is reached at  $y = 0$ , and the flux decreases monotonically toward the Jupiter-facing and Jupiter-averted edges of the interaction region. Also, taking a look at the different ranges of the vertical axis in the three plots illustrates that the ionospheric conductance peak is able to prevent the bulk of the flow’s kinetic energy from ever

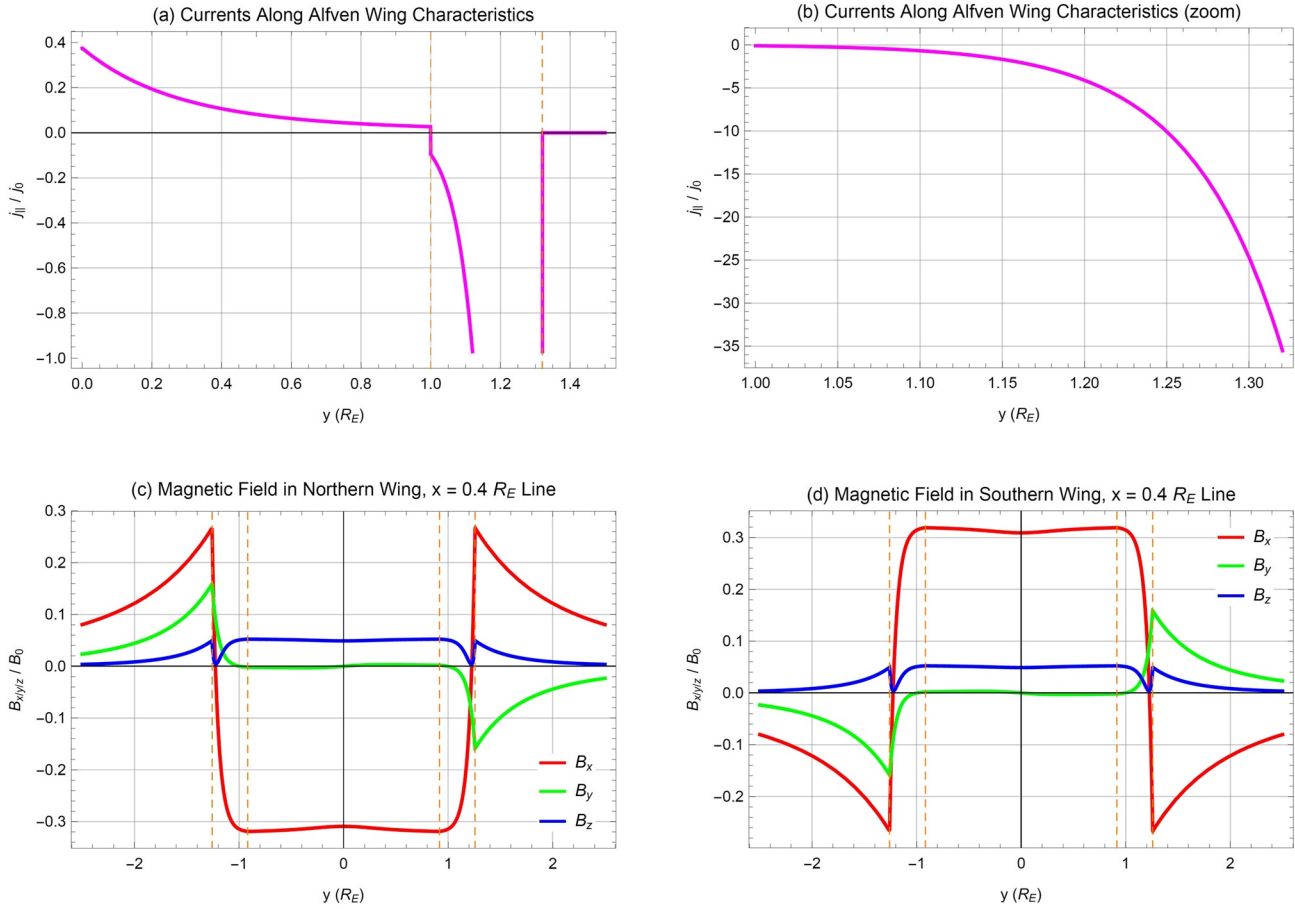


**Figure 6.** (a) Currents  $j_{\parallel}$  along the southern Alfvén wing characteristic, as calculated from Equation 25 for the positive  $y$ -axis ( $\phi = 90^\circ$ ). (b) Magnified depiction of the wing-aligned currents from panel (a) between  $y = R_1 = R_E$  and  $y = R_2 \approx 1.32R_E$ . The current densities in both panels are expressed in units of  $j_0 = \Sigma_A E_0 / R_E$ . Please note that in panel (a), the vertical axis covers a much smaller range of values than in panel (b). There is *no physical gap* in the current density in panel (a) around  $y = 1.2R_E$ . (c) Magnetic field perturbations  $B_x$  (red),  $B_y$  (green), and  $B_z$  (blue) along a cut through the northern Alfvén wing at  $x = 0.4R_E$ . All values are normalized to the background field strength  $B_0$ . Also, the field components shown in the plot have been detrended by subtracting the background field vector  $\vec{B}_0$ . Therefore, the baseline for all three field components is  $B_{x,y,z} = 0$  and only the perturbations caused by the Alfvén wing are shown. (d) Same as panel (c) for a cut through the southern Alfvén wing at  $x = 0.4R_E$ . The orange, dashed lines in panels (a), (c), and (d) denote the locations where the (horizontal)  $y$ -axis intersects the inner ( $r = R_E$ ) and outer ( $r = R_2$ ) cylinder mantles of the ionospheric conductance profile.

reaching the surface at  $r = 1R_E$ : The peak energy flux in Figure 5a is a factor of 500 smaller than the maximum energy flux associated with the undisturbed upstream flow.

The precise location where the transition from an “M-like” (see Figures 5b and 5c) to a “bullseye-like” (see Figure 5a) energy deposition pattern takes place is determined by the specific parameters of the ionospheric conductance profile. For an interaction strength  $\alpha \ll 1$ , the streamlines of the impinging plasma would still be bent near the innermost cylinder and would give rise to an “M”-like energy deposition pattern, similar to that displayed in Figures 5b and 5c. Also, we again note that our results illustrate only how the Alfvénic field perturbations alone affect the energy flux pattern. However, our findings emphasize that the spatial distribution of the energy influx may change drastically between the top of a moon’s exosphere (where it can contribute to excitation or ionization of neutrals) and its surface (where it can contribute to weathering).

### 3.5. Currents Along the Alfvén Wing Characteristics and Magnetic Field

We now further investigate the properties of the wing-aligned currents  $j_{\parallel}$ , as already briefly addressed in Section 2.2. For this purpose, Figures 6a and 6b display the currents along the southern Alfvén wing for a cut along the positive  $y$ -axis. According to Equation 25 the magnitude of the currents is maximized along

the  $y$ -axis ( $\phi = \pm 90^\circ$ ), due to the absence of the ionospheric Hall effect (Simon, Saur, Kriegel, et al., 2011; Simon, Saur, Neubauer, et al., 2011). As can be seen, the strength of the currents powering the Alfvén wing spans several orders of magnitude. Within the Europa fluxtube  $|y| \leq R_E$ , the maximum strength of  $j_{\parallel}$  reaches only about 1% of the peak value outside of the fluxtube (see Figures 6a and 6b). For the parameters chosen here, the inner region of the Europa fluxtube (where  $\Sigma_p(r)$  increases monotonically) is almost devoid of currents, and the bulk of the wing-aligned currents is bundled outside of the fluxtube where the conductance falls off with distance to the  $z$ -axis. In other words, the “spike” in the ionospheric conductance profile at  $r = R_E$  efficiently prevents the inner part of the ionosphere ( $r \leq R_E$ ) from establishing a strong coupling to Jupiter’s polar ionosphere through wing-aligned currents. A plethora of additional processes occur until the wing-aligned currents ultimately reach Jupiter’s polar ionosphere, such as partial reflection at the outer boundaries of the Europa torus and turbulent filamentation of the Alfvén waves (e.g., Chust et al., 2005; Hess et al., 2011). However, it may be interesting to investigate whether any of these radial non-uniformities in the wing-aligned current profile ultimately map into observable features of the moon’s auroral footprint morphology.

As shown in Figure 6a, two discontinuities are visible in the wing-aligned current system. At  $r = R_E$ , the current  $j_{\parallel}$  jumps from positive to negative values, whereas it subsequently remains negative for increasing distance and then sharply drops to zero at the outer edge of the exosphere (here:  $y = r = R_2$ ). Thus, continuity of the ionospheric conductance profile does *not* ensure continuity of the wing-aligned current systems, especially not at the obstacle’s outer boundary. The direction of the wing-aligned currents is determined by the slope of  $\Sigma_p(r)$  in the respective region. As can be seen from Figure 6a,  $j_{\parallel}$  along the chosen cut is positive where  $\Sigma_p(r)$  increases with distance  $r$  to the  $z$ -axis and negative where  $\Sigma_p(r)$  decreases. Overall, the shape of the  $|j_{\parallel}|$  distribution in regions I and II is exactly *opposite* to that of the ionospheric conductance profile: The magnitude of the currents *increases* with distance  $r$  in regions where  $\Sigma_p(r)$  *decreases* and vice versa. Most importantly, the wing-aligned currents do *not* reach their maximum strength at the location  $r = R_E$  of the ionospheric conductance peak, as proposed by Blöcker et al. (2016) (see page 9,802 in that work). We emphasize that none of these fine structures in the wing-aligned current systems are captured by earlier iterations of the analytical model that treat the ionospheric conductance profile as piecewise constant (e.g., Saur et al., 2007; Simon, Saur, Kriegel, et al., 2011; Simon, Saur, Neubauer, et al., 2011). In these preceding versions of the model, the wing-aligned currents were bundled in a delta-like fashion at the interfaces between consecutive plateaus in the conductance profile. In regions with a constant value of  $\Sigma_p$ , the modeled potential  $\psi$  was a harmonic function, that is, according to Equation 24 they were devoid of any wing-aligned currents.

The perturbations in the magnetic field components associated with the Alfvénic interaction are shown in Figures 6c and 6d. In these plots, we display cuts along the  $x = 0.4R_E$  line and *not* along the  $y$ -axis: Due to the absence of the ionospheric Hall effect in our model calculations, the perturbations in the  $B_y$  component are exactly zero along the  $y$ -axis (Simon, Saur, Kriegel, et al., 2011; Simon, Saur, Neubauer, et al., 2011). A detailed analysis of the magnetic signatures generated by sub-Alfvénic moon-plasma interactions has already been provided in our preceding publications (Simon, 2015; Simon, Saur, Kriegel, et al., 2011; Simon, Saur, Neubauer, et al., 2011). Therefore, we restrict the discussion to pointing out several important features of the magnetic signatures that were not captured (or not explicitly addressed) by preceding studies.

The outer boundary of the obstacle ( $r = R_2$ ) intersects the  $x = 0.4R_E$  line at  $y = \pm 1.26R_E$ . As can be seen from Figures 6c and 6d, the strong jump in the wing-aligned currents at that location gives rise to clearly discernible spikes in the magnetic field components of both wings. In preceding iterations of the model that treated the ionospheric conductance profile as box-like, these spikes were inseparable from the magnetic field jumps generated by the discontinuous drop in ionospheric Pedersen conductance at the outer boundary of the obstacle (e.g., Saur et al., 2007; Simon, Saur, Kriegel, et al., 2011; Simon, Saur, Neubauer, et al., 2011). However, the more detailed Pedersen conductance profile applied here reveals that there are actual physical “spikes” present in the magnetic field at the outer boundary of the obstacle. We emphasize that these structures are *not* (rotational) discontinuities: All three magnetic field components are continuous at  $r = R_2$ ; only their first derivative (i.e., the current) jumps.

Due to the translational symmetry of the Alfvén wings along the respective characteristics, these spikes would still be discernible in the magnetic field at large distances to the moon. In other words, magnetic

field observations from distant crossings through a moon's Alfvén wing are highly suitable to constrain the “effective” size of the obstacle that its ionosphere represents to the impinging magnetospheric flow. As can be inferred from Equation 25, the magnitude of these spikes varies with longitude  $\phi$  along the outer surface ( $r = R_2$ ) of the moon's Alfvén wings. Therefore, a spacecraft flyby must still have a “favorable” geometry to capture these signatures among the multitude of effects that shape a moon's intermediate or distant magnetic environment. For the set of upstream and obstacle parameters chosen here, the jump in the wing-aligned current systems at  $r = R_E$  is much weaker than at  $r = R_2$  (see Figure 6a). Therefore, there are no strong “spikey” signatures discernible in the magnetic field components at  $r = R_E$  (corresponding to  $y = \pm 0.92R_E$  in Figure 6a). However, for a different set of ionospheric parameters, the spikes at  $r = R_1$  and  $r = R_2$  may be of comparable magnitude (see Figure A1 in Simon, 2015).

As expected, Figures 6a and 6b show that the draped magnetic field has a negative  $B_x$  component in the central region of the northern wing and a positive  $B_x$  component within the southern wing. The Alfvénic magnetic field perturbations can be described by a two-dimensional magnetic dipole moment perpendicular to the wing characteristics (Neubauer, 1980). In order for these dipolar field lines to close, the  $B_x$  component needs to reverse its sign outside of the moon's fluxtube (see also Figure 8 in Simon, Saur, Kriegel, et al., 2011; for an illustration). To the authors' knowledge, this “anti-draping” of the magnetic field (i.e.,  $B_x > 0$  in the northern hemisphere and  $B_x < 0$  in the southern hemisphere) has so far been observed only during very few Cassini flybys of Titan (Simon, van Treeck, et al., 2013). As illustrated in Figures 6c and 6d, the “anti-draping” of the field lines in both wings already commences within the descending flank of the moon's ionospheric conductance profile and is not restricted to the region outside of the obstacle ( $r > R_2$ ).

Only during a single, non-targeted flyby (nicknamed E25A, see Blöcker et al., 2016) did the Galileo spacecraft travel through Europa's distant, northern Alfvén wing. We note that the strength of the magnetic draping signature observed during that wing crossing (about  $\Delta B_x \approx 0.2B_0$ , see Figure 11 of Blöcker et al., 2016) is similar to that from our model (see Figure 6). However, during E25A Europa did possess a strong induced magnetic moment, which may explain why the observed draping signature was somewhat weaker than the modeled perturbation: As shown by Neubauer (1999), the presence of an induced magnetic field reduces the currents along the Alfvén characteristics, compared to a pure ionosphere-magnetosphere interaction.

### 3.6. Poynting Flux

We now take a brief look at the Poynting flux  $\underline{S} = \underline{E} \times \underline{B} / \mu_0$  radiated away along the Alfvén wing characteristics. Since the electric field is not invariant under the Galilean transformation, this quantity depends on the frame of reference in which the fields are defined. To facilitate comparison to the results of Saur et al. (2013) and Simon, Kriegel, et al. (2013), we proceed in analogy to these two studies and choose a reference frame that moves synchronously with the upstream flow at velocity  $\underline{u}_0$ . Using Equations 10–12 of Simon, Kriegel, et al. (2013), we find

$$S_{z,i} = \frac{1}{\mu_0} \left\{ B_y \frac{\partial \psi_i}{\partial x} - B_x \left( \frac{\partial \psi_i}{\partial y} - u_0 B_z \right) \right\} ; \quad i = I, II, III \quad (38)$$

for the electromagnetic energy flux along the Alfvén characteristics  $\pm \underline{e}_z$ .

Figure 7 displays the spatial distribution of the Poynting flux for a cut  $z = \text{const}$  through the northern Alfvén wing. As can be seen, the value of  $S_z$  is largest (and nearly constant) within the center  $r \leq R_2$  of the interaction region. Outside of Europa's exosphere, significant amounts of electromagnetic energy are also irradiated away from the moon near the upstream and downstream apices. Most remarkably, however, Figure 7 reveals that the Poynting flux near Europa may assume both, positive and negative signs. Specifically, localized regions with  $S_z < 0$  are formed along the Jupiter-facing and Jupiter-averted flanks of the interaction region. As revealed by Figure 7 (and also by Figures 8c and 8d of Simon, Saur, Kriegel, et al., 2011; Simon, Saur, Neubauer, et al., 2011), the reversal in the direction of the Poynting flux occurs in regions where the magnetic field is “anti-draped” to ensure closure of the field lines in planes perpendicular to the wing characteristics. While the net Poynting flux is positive (i.e., directed away from Europa), the results shown

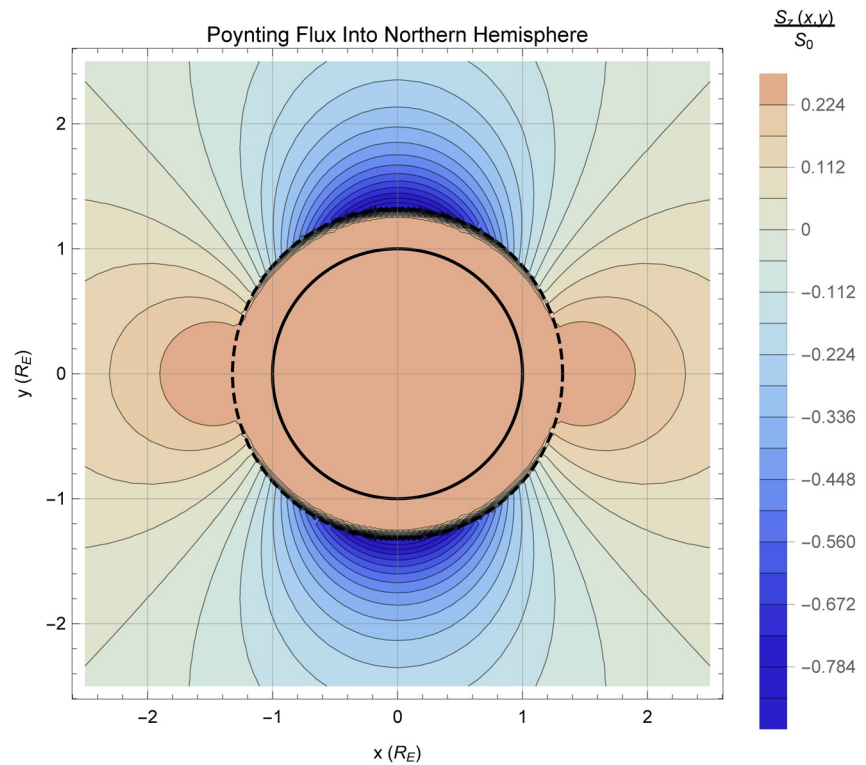


**Figure 7.** Poynting flux through a plane  $z = \text{const}$  perpendicular to the northern Alfvén wing characteristic. The “upstream” energy flux  $S_0 = E_0 B_0 / \mu_0$  has been used for normalization. The solid and dashed black circles denote the projections of Europa ( $r = R_1 = R_E$ ) and the outer boundary of the moon’s exosphere ( $r = R_2$ ) onto the cutting plane, respectively. Reddish hue denotes regions where the Poynting flux is directed away from Europa ( $S_z > 0$ ), while blue represents regions where the flux is directed toward the moon ( $S_z < 0$ ).

in Figure 7 reveal that the spatial pattern of the energy flux is way more complex than suggested by preceding models that treated the ionospheric obstacle as box-like (Saur et al., 2013; Simon, Kriegel, et al., 2013).

Depending on the density and composition of a moon’s exosphere, this localized “return flow” of electromagnetic energy along the Alfvén characteristics may contribute to the energization of exospheric neutrals. However, as said, multiple additional processes take place along the magnetic pathway between the moon and its parent planet (e.g., Chust et al., 2005; Hess et al., 2011). These processes need to be carefully evaluated in order to obtain any quantitative constraints on the magnitude of this “returning” energy flux and its influence on the local moon-magnetosphere interaction.

#### 4. Summary and Concluding Remarks

The goal of this study was to explore the fundamental physics of sub-Alfvénic moon-magnetosphere interactions for a realistic, “suspension bridge”-like Pedersen conductance profile in the object’s ionosphere. For this purpose, we have analytically calculated the electrostatic potential  $\psi$  near the Alfvén wings for a conductance profile composed of a sequence of exponential functions with alternating slopes. The potential  $\psi$  determines several other key quantities of the interaction, such as the magnetic field perturbations and associated currents, the bulk velocity  $\underline{u}$  of the magnetospheric plasma, the number and kinetic energy flux deposited by the flow onto the moon’s surface as well as the Poynting flux along the Alfvén characteristics.

Including the new solution developed here for an exponential conductance profile, there are now three different approaches available to analytically determine the potential  $\psi$  of the Alfvénic interaction:

- (i) Representation of the ionosphere through piecewise constant, “box-like” conductance profiles (e.g., Blöcker et al., 2016; Saur et al., 2007; Simon, Saur, Kriegel, et al., 2011; Simon, Saur, Neubauer, et al., 2011). The advantage of this class of solutions is that it captures any asymmetries in the flow pattern and magnetic field caused by the ionospheric Hall effect. A major disadvantage of this type of solution is that it contains artificial rotational discontinuities in the magnetic field wherever the ionospheric Pedersen and Hall conductances change their values.
- (ii) Description of the ionospheric conductance profile through a sequence of power laws (Simon, 2015). While this approach provides a representation of the magnetic field perturbations in the Alfvén wings that is not “contaminated” by artificial discontinuities, it is not able to reproduce asymmetries in the interaction due to the ionospheric Hall effect.
- (iii) Representation of the “suspension bridge”-like Pedersen conductance profile through a sequence of exponential functions. This approach is able to capture steeper gradients in the conductance profile than method (ii), which may facilitate adaption of the model to actual observations of the ionospheric conductance distribution. Methods (ii) and (iii) are subject to the same limitations.

By applying the exponential form (iii) of the ionospheric Pedersen conductance, we have arrived at the following general conclusions on the physics of sub-Alfvénic moon-magnetosphere interactions:

1. Deflection of the incident thermal plasma around the moon’s Alfvén wings may significantly reduce the number flux of the magnetospheric flow onto the surface. However, while the Alfvénic interaction alone depletes the net value of the incident flux, it does not alter the overall shape of the flux pattern: With the Alfvénic perturbations included, the precipitating number flux still peaks at the moon’s ramside apex and decreases monotonically toward the planet-facing and planet-averted flanks of the interaction region.
2. The overall morphology of the kinetic energy flux carried by impinging thermal ions drastically changes as a function of distance to the moon. In the unperturbed upstream region, the energy flux onto a cylindrical/circular obstacle peaks at the ramside apex and decreases monotonically with distance from that location. At intermediate distances where flow deflection around the Alfvén wings has already commenced, the energy flux minimizes at the ramside apex and forms two symmetric maxima at the planet-facing and planet-averted flanks of the interaction region. In the “core region” of the Alfvén wing encapsulating the moon, the strongly depleted energy flux again resumes its original pattern and peaks above the ramside apex. The bulk of the energy flux cannot even reach altitudes below the ionospheric conductance peak. While our model calculations can describe only the behavior of the thermal magnetospheric flow in absence of gyration effects, these considerations are highly relevant when analyzing surface weathering features at icy moons. For instance, the discrimination between magnetospheric energy flux and number flux onto Europa’s surface was suggested to be important in explaining the spatial distribution of sulfuric acid deposits at Europa (Dalton et al., 2013).
3. Although the ionospheric Pedersen conductance profile  $\Sigma_P(r)$  is continuous, discontinuities are formed in the wing-aligned currents at locations where the slope of  $\Sigma_P(r)$  changes its sign and also, at the outer edge of the moon’s ionosphere where the Pedersen conductance drops to zero. These jumps in the wing-aligned current system give rise to observable spikes in all three magnetic field components. Since these signatures can still be detected at large distances to the moon, they may help to constrain the “effective” extension of the obstacle to the flow through magnetic field observations from distant flybys through the Alfvén wing tubes. The sign of the first derivative  $\frac{d\Sigma_P(r)}{dr}$  also determines the magnitude and direction of the wing-aligned currents (toward/away from the moon) in the respective region.
4. In localized regions near the wing tubes, the Poynting flux generated by the Alfvénic interaction may be directed toward the obstacle and not away from it.

In a case study, we have applied the analytical model to analyze key properties of Europa’s plasma environment. In contrast to numerical models of Europa’s magnetospheric interaction, our analytical approach does not take into account the contribution of local ionospheric currents to the flow deflection. These currents generate, for example, the magnetic pile-up region at the moon’s ramside. However, a recent study by Addison et al. (2021) revealed that deflection of the upstream thermal plasma through the gradient drift in the pile-up region has only minimal quantitative influence on the flow deflection and the resulting surface precipitation pattern. In both, our analytical model and the (more complex) numerical approach of

Addison et al. (2021), the equatorial surface flux is about 1–2 orders of magnitude lower than the thermal ion flux outside the interaction region. In addition, both models reveal the surface flux of thermal ions to decrease longitudinally with distance from the ramside apex. The assumption of a symmetric flow pattern between the Jupiter-facing and Jupiter-averted hemispheres (corresponding to  $\Sigma_H = 0$ ) is also well justified at Europa. Therefore, the number and energy fluxes provided by the analytical model can be considered an adequate description of thermal ion precipitation onto Europa's surface near *equatorial* latitudes. We note that the  $\Sigma_p \gg \Sigma_H$  criterion is also applicable at Rhea (Simon et al., 2012), various exoplanets exposed to sub-Alfvénic stellar wind (Saur et al., 2013), and Ganymede (Kivelson et al., 2004), although this moon's plasma interaction is complicated by its internal magnetic field.

While only a single, non-targeted Europa flyby of the Galileo spacecraft intersected the moon's distant Alfvén wings, there will hopefully be more of these events during the upcoming flybys of Juno, Europa Clipper, and JUICE. If such flybys take place while the induced field from Europa's interior is weak, our analytical model is able to quantitatively emulate the magnetic signatures observable during these events. Therefore, the plasma and energy flux patterns as well as the magnetic signatures obtained from our model have immediate relevance for the interpretation of spacecraft observations at Europa.

## Appendix A: Derivation of the Analytical Solution for the Electric Potential Equation

The solution 6 of the radial potential Equation 5 for an exponential conductance profile has been determined using the *Wolfram Alpha* knowledge engine. In the following, we provide a detailed derivation of this solution. We start by introducing a function  $f(r)$  according to

$$\Lambda(r) = \frac{f(r)}{r^2} \quad (\text{A1})$$

and insert this ansatz into Equation 5. This yields

$$f(r) \frac{3-2\beta r}{r^4} + \frac{df(r)}{dr} \frac{\beta r-3}{r^3} + \frac{d^2 f(r)}{dr^2} \frac{1}{r^2} = 0. \quad (\text{A2})$$

Making use of

$$\frac{3-2\beta r}{r^4} = \frac{d}{dr} \left( \frac{\beta r-3}{r^3} \right) - \frac{d^2}{dr^2} \left( \frac{1}{r^2} \right) \quad (\text{A3})$$

allows us to rewrite Equation A2 according to

$$\frac{1}{r^2} \frac{d^2 f(r)}{dr^2} + \frac{\beta r-3}{r^3} \frac{df(r)}{dr} + f(r) \left\{ \frac{d}{dr} \left( \frac{\beta r-3}{r^3} \right) - \frac{d^2}{dr^2} \left( \frac{1}{r^2} \right) \right\} = 0. \quad (\text{A4})$$

This equation can be rewritten as

$$\frac{d}{dr} \left\{ \frac{1}{r^2} \frac{df(r)}{dr} + \frac{\beta r-1}{r^3} f(r) \right\} = 0, \quad (\text{A5})$$

or equivalently,

$$\frac{df(r)}{dr} + \left( \beta - \frac{1}{r} \right) f(r) = C_1 r^2, \quad (\text{A6})$$

where  $C_1$  is a constant of integration. Multiplying both sides of this expression with  $\exp(\beta r) / r$  then leads to

$$\frac{d}{dr} \left( \frac{\exp(\beta r)}{r} f(r) \right) = C_1 \exp(\beta r) r. \quad (\text{A7})$$

Another integration now produces the desired solution for  $f(r)$ :

$$f(r) = \frac{C_1 r}{\beta^2} (\beta r - 1) + C_2 r \exp(-\beta r) \quad (\text{A8})$$

with a second constant of integration  $C_2$ . We now introduce new constants  $K_1$  and  $K_2$  through

$$K_1 = \frac{C_1}{\beta^2} \quad \text{and} \quad K_2 = C_2, \quad (\text{A9})$$

which yields the final form of our solution:

$$f(r) = K_1 r (\beta r - 1) + K_2 r \exp(-\beta r). \quad (\text{A10})$$

Inserting this expression into Equation A1 then leads to the general solution

$$\Lambda(r) = \frac{K_1 (\beta r - 1) + K_2 \exp(-\beta r)}{r}, \quad (\text{A11})$$

as given in Equation 6.

## Data Availability Statement

The model calculations presented in this study have been carried out using the Wolfram Mathematica software. All plotting routines, graphics, and datasets shown in this manuscript are embedded in the Mathematica script, an annotated version of which can be downloaded at <https://doi.org/10.5281/zenodo.4409281>. The source code provided at that link can easily be adapted to any other interaction scenario between a sub-Alfvénic plasma flow and a planetary moon's (or an exoplanet's) ionosphere.

## Acknowledgments

S. Simon appreciates the thoughtful guidance and patience of Fritz M. Neubauer and Joachim Saur (University of Cologne) when introducing him to the analytical interaction model. The authors are grateful to the NASA Solar System Workings program (grants # 80NSSC20K0463 and # 80NSSC21K0152) for financial support.

## References

- Addison, P., Liuzzo, L., Arnold, H., & Simon, S. (2021). Influence of Europa's time-varying electromagnetic environment on magnetospheric ion precipitation and surface weathering. *Journal of Geophysical Research: Space Physics*, 126(5), e2020JA029087. <https://doi.org/10.1029/2020JA029087>
- Arnold, H., Liuzzo, L., & Simon, S. (2019). Magnetic signatures of a plume at Europa during the Galileo E26 Flyby. *Geophysical Research Letters*, 46(3), 1149–1157. <https://doi.org/10.1029/2018GL081544>
- Arnold, H., Liuzzo, L., & Simon, S. (2020). Plasma interaction signatures of plumes at Europa. *Journal of Geophysical Research: Space Physics*, 125(1), e2019JA027346. <https://doi.org/10.1029/2019JA027346>
- Arridge, C. S., André, N., Bertucci, C. L., Garnier, P., Jackman, C. M., Németh, Z., et al. (2011). Upstream of Saturn and Titan. *Space Science Reviews*, 162(1–4), 25–83. <https://doi.org/10.1007/s11214-011-9849-x>
- Bagenal, F., & Delamere, P. A. (2011). Flow of mass and energy in the magnetospheres of Jupiter and Saturn. *Journal of Geophysical Research*, 116(A5), A05209. <https://doi.org/10.1029/2010JA016294>
- Blöcker, A., Saur, J., & Roth, L. (2016). Europa's plasma interaction with an inhomogeneous atmosphere: Development of Alfvén winglets within the Alfvén Wings. *Journal of Geophysical Research*, 121(10), 9794–9828. <https://doi.org/10.1002/2016JA022479>
- Blöcker, A., Saur, J., Roth, L., & Strobel, D. F. (2018). Mhd modeling of the plasma interaction with Io's asymmetric atmosphere. *Journal of Geophysical Research: Space Physics*, 123(11), 9286–9311. <https://doi.org/10.1029/2018JA025747>
- Breer, B. R., Liuzzo, L., Arnold, H., Andersson, P. N., & Simon, S. (2019). Energetic Ion Dynamics in the Perturbed Electromagnetic Fields near Europa. *Journal of Geophysical Research: Space Physics*, 124(9), 7592–7613. <https://doi.org/10.1029/2019JA027147>
- Cassidy, T. A., Paranicas, C. P., Shirley, J. H., Dalton, J. B., III, Teolis, B. D., Johnson, R. E., et al. (2013). Magnetospheric ion sputtering and water ice grain size at Europa. *Planetary and Space Science*, 77, 64–73. <https://doi.org/10.1016/j.pss.2012.07.008>
- Chust, T., Roux, A., Kurth, W. S., Gurnett, D. A., Kivelson, M. G., & Khurana, K. K. (2005). Are Io's Alfvén wings filamented? Galileo observations. *Planetary and Space Science*, 53(4), 395–412. <https://doi.org/10.1016/j.pss.2004.09.021>
- Cooper, J. F., Johnson, R. E., Mauk, B. H., Garrett, H. B., & Gehrels, N. (2001). Energetic ion and electron irradiation of the icy Galilean satellites. *Icarus*, 149(1), 133–159. <https://doi.org/10.1006/icar.2000.6498>

- Dalton, J. B., Cassidy, T., Paranicas, C., Shirley, J. H., Prockter, L. M., & Kamp, L. W. (2013). Exogenic controls on sulfuric acid hydrate production at the surface of Europa. *Europa Planetary and Space Science*, 77, 45–63. <https://doi.org/10.1016/j.pss.2012.05.013>
- Hartkorn, O., & Saur, J. (2017). Induction signals from Callisto's ionosphere and their implications on a possible subsurface ocean. *Journal of Geophysical Research: Space Physics*, 122(11), 11677–11697. <https://doi.org/10.1002/2017JA024269>
- Hartkorn, O., Saur, J., & Strobel, D. F. (2017). Structure and density of Callisto's atmosphere from a fluid-kinetic model of its ionosphere: Comparison with Hubble Space Telescope and Galileo observations. *Icarus*, 282, 237–259. <https://doi.org/10.1016/j.icarus.2016.09.020>
- Hess, S. L. G., Delamere, P. A., Dols, V., & Ray, L. C. (2011). Comparative study of the power transferred from satellite-magnetosphere interactions to auroral emissions. *Journal of Geophysical Research*, 116(A1), A01202. <https://doi.org/10.1029/2010JA015807>
- Jia, X., Kivelson, M. G., Khurana, K. K., & Kurth, W. S. (2018). Evidence of a plume on Europa from Galileo magnetic and plasma wave signatures. *Nature Astronomy*, 2, 459–464. <https://doi.org/10.1038/s41550-018-0450-z>
- Johnson, R. E., Burger, M. H., Cassidy, T. A., Leblanc, F., Marconi, M., & Smyth, W. H. (2009). Composition and detection of Europa's sputter-induced atmosphere. In R. T. Pappalardo, W. B. McKinnon, & K. K. Khurana (Eds.), *Europa, Edited By Robert T. Pappalardo, William B. Mckinnon, Krishan K. Khurana; With the Assistance of René Dotson With 85 Collaborating Authors. University Of Arizona Press, Tucson, 2009. The University Of Arizona Space Science Series* (ISBN: 9780816528448, p. 507).
- Khurana, K. K., Fatemi, S., Lindkvist, J., Roussos, E., Krupp, N., Holmström, M., et al. (2017). The role of plasma slowdown in the generation of Rhea's Alfvén wings. *Journal of Geophysical Research: Space Physics*, 122(2), 1778–1788. <https://doi.org/10.1002/2016JA023595>
- Kivelson, M. G., Bagenal, F., Kurth, W. S., Neubauer, F. M., Paranicas, C., & Saur, J. (2004). Magnetospheric interactions with satellites. In F. Bagenal, T. E. Dowling, & W. B. McKinnon (Eds.), *Jupiter: The planet, Satellites and Magnetosphere* (pp. 513–536). Cambridge University Press.
- Kivelson, M. G., Khurana, K. K., Stevenson, D. J., Bennett, L., Joy, S., Russell, C. T., et al. (1999). Europa and Callisto: Induced or intrinsic fields in a periodically varying plasma environment. *Journal of Geophysical Research*, 104(A3), 4609–4625. <https://doi.org/10.1029/1998JA900095>
- Kivelson, M. G., Khurana, K. K., & Volwerk, M. (2002). The Permanent and Inductive Magnetic Moments of Ganymede. *Icarus*, 157(2), 507–522. <https://doi.org/10.1006/icar.2002.6834>
- Kivelson, M. G., Khurana, K. K., & Volwerk, M. (2009). Europa's Interaction with the Jovian Magnetosphere. In R. T. Pappalardo, W. B. McKinnon, & K. K. Khurana (Eds.), *Europa, Edited by Robert T. Pappalardo, William B. Mckinnon, Krishan K. Khurana; With the Assistance of René Dotson With 85 Collaborating Authors. University Of Arizona Press, Tucson, 2009. The University Of Arizona Space Science Series* (ISBN: 9780816528448, p. 545).
- Kliore, A. J., Hinson, D. P., Flasar, F. M., Nagy, A. F., & Cravens, T. E. (1997, July). The ionosphere of Europa from Galileo radio occultations. *Science*, 277, 355–358. <https://doi.org/10.1126/science.277.5324.355>
- Kriegel, H., Simon, S., Meier, P., Motschmann, U., Saur, J., Wennmacher, A., et al. (2014). Ion densities and magnetic signatures of dust pick-up at Enceladus. *Journal of Geophysical Research*, 119(4), 2740–2774. <https://doi.org/10.1002/2013JA019440>
- Kriegel, H., Simon, S., Motschmann, U., Saur, J., Neubauer, F. M., Persoon, A. M., et al. (2011). Influence of negatively charged plume grains on the structure of Enceladus' Alfvén wings: Hybrid simulations versus Cassini MAG data. *Journal of Geophysical Research*, 116(A10), A10223. <https://doi.org/10.1029/2011JA016842>
- Krupp, N., Kotova, A., Roussos, E., Simon, S., Liuzzo, L., Paranicas, C., et al. (2020). Magnetospheric interactions of Saturn's Moon Dione (2005–2015). *Journal of Geophysical Research: Space Physics*, 125(6), e2019JA027688. <https://doi.org/10.1029/2019JA027688>
- Kurth, W. S., Gurnett, D. A., Persoon, A. M., Roux, A., Bolton, S. J., & Alexander, C. J. (2001). The plasma wave environment of Europa. *Europa Planetary and Space Science*, 49, 345–363. [https://doi.org/10.1016/S0032-0633\(00\)00156-2](https://doi.org/10.1016/S0032-0633(00)00156-2)
- Liuzzo, L., Feyerabend, M., Simon, S., & Motschmann, U. (2015). The impact of Callisto's atmosphere on its plasma interaction with the Jovian magnetosphere. *Journal of Geophysical Research: Space Physics*, 120, 9401–9427. <https://doi.org/10.1002/2015JA021792>
- Liuzzo, L., Simon, S., & Feyerabend, M. (2018). Observability of Callisto's inductive signature during the JUPITER ICY moons Explorer mission. *Journal of Geophysical Research: Space Physics*, 123, 9045–9054. <https://doi.org/10.1002/2018JA025951>
- Liuzzo, L., Simon, S., Feyerabend, M., & Motschmann, U. (2016). Disentangling plasma interaction and induction signatures at Callisto: The Galileo C10 flyby. *Journal of Geophysical Research: Space Physics*, 121(9), 8677–8694. <https://doi.org/10.1002/2016JA023236>
- Liuzzo, L., Simon, S., & Regoli, L. (2019a). Energetic electron dynamics near Callisto. *Planetary and Space Science*, 179, 104726. <https://doi.org/10.1016/j.pss.2019.104726>
- Liuzzo, L., Simon, S., & Regoli, L. (2019b). Energetic ion dynamics near Callisto. *Planetary and Space Science*, 166, 23–53. <https://doi.org/10.1016/j.pss.2018.07.014>
- Mauk, B., Mitchell, D., McEntire, R., Paranicas, C., Roelof, E., Williams, D., & Lagg, A. (2004). Energetic ion characteristics and neutral gas interactions in Jupiter's magnetosphere. *Journal of Geophysical Research*, 109(A9). <https://doi.org/10.1029/2003JA010270>
- Neubauer, F. M. (1980). Nonlinear standing Alfvén wave current system at Io – Theory. *Journal of Geophysical Research*, 85, 1171–1178. <https://doi.org/10.1029/JA085iA03p01171>
- Neubauer, F. M. (1998). The sub-Alfvénic interaction of the Galilean satellites with the Jovian magnetosphere. *Journal of Geophysical Research*, 103, 19843–19866. <https://doi.org/10.1029/97JE03370>
- Neubauer, F. M. (1999). Alfvén wings and electromagnetic induction in the interiors: Europa and Callisto. *Journal of Geophysical Research*, 104(A12), 28671–28684. <https://doi.org/10.1029/1999JA900217>
- Neubauer, F. M., Backes, H., Dougherty, M. K., Wennmacher, A., Russell, C. T., Coates, A., et al. (2006). Titan's near magnetotail from magnetic field and plasma observations and modeling: Cassini flybys TA, TB and T3. *Journal of Geophysical Research*, 111, A10220. <https://doi.org/10.1029/2006JA011676>
- Neubauer, F. M., Gurnett, D. A., Scudder, J. D., & Hartle, R. E. (1984). Titan's magnetospheric interaction. In T. Gehrels, & M. S. Matthews (Eds.), *Saturn* (pp. 760–787). University of Arizona Press.
- Paranicas, C., Cooper, J. F., Garrett, H. B., Johnson, R. E., & Sturner, S. J. (2009). Europa's radiation environment and its effects on the surface. In R. T. Pappalardo, W. B. McKinnon, & K. K. Khurana (Eds.), *Europa, Edited by Robert T. Pappalardo, William B. Mckinnon, Krishan K. Khurana; With the Assistance of René Dotson With 85 Collaborating Authors. University Of Arizona Press, Tucson, 2009. The University Of Arizona Space Science Series* (ISBN: 9780816528448, p. 529).
- Paranicas, C., McEntire, R. W., Cheng, A. F., Lagg, A., & Williams, D. J. (2000). Energetic charged particles near Europa. *Journal of Geophysical Research*, 105, 16005–16015. <https://doi.org/10.1029/1999JA000350>
- Plainaki, C., Milillo, A., Mura, A., Saur, J., Orsini, S., & Massetti, S. (2013, November). Exospheric O<sub>2</sub> densities at Europa during different orbital phases. *Planetary and Space Science*, 88, 42–52. <https://doi.org/10.1016/j.pss.2013.08.011>
- Poppe, A. R., Fatemi, S., & Khurana, K. K. (2018). Thermal and energetic ion dynamics in Ganymede's magnetosphere. *Journal of Geophysical Research: Space Physics*, 123, 4614–4637. <https://doi.org/10.1029/2018JA025312>

- Pospieszalska, M. K., & Johnson, R. E. (1989). March). Magnetospheric ion bombardment profiles of satellites – Europa and Dione. *Icarus*, 78, 1–13. [https://doi.org/10.1016/0019-1035\(89\)90065-1](https://doi.org/10.1016/0019-1035(89)90065-1)
- Regoli, L., Roussos, E., Feyerabend, M., Jones, G. H., Krupp, N., Coates, A. J., et al. (2016). Access of energetic particles to Titan’s exobase: A study of Cassini’s t9 flyby. *Planetary and Space Science*, 130, 40–53. <https://doi.org/10.1016/j.pss.2015.11.013>
- Roth, L., Retherford, K. D., Saur, J., Strobel, D. F., Feldman, P. D., McGrath, M. A., & Nimmo, F. (2014). Orbital apocenter is not a sufficient condition for HST/STIS detection of Europa’s water vapor aurora. *Proceedings of the National Academy of Sciences*, 111, E5123–E5132. <https://doi.org/10.1073/pnas.1416671111>
- Roth, L., Saur, J., Retherford, K. D., Strobel, D. F., Feldman, P. D., McGrath, M. A., & Nimmo, F. (2014). Transient water vapor at Europa’s south pole. *Science*, 343(6167), 171–174. <https://doi.org/10.1126/science.1247051>
- Roussos, E., Mueller, J., Simon, S., Boesswetter, A., Motschmann, U., Krupp, N., et al. (2008). Plasma and fields in the wake of Rhea: 3-D hybrid simulation and comparison with Cassini data. *Annales Geophysicae*, 26(3), 619–637. <https://doi.org/10.5194/angeo-26-619-2008>
- Rubin, M., Jia, X., Altwegg, K., Combi, M. R., Daldorff, L. K. S., Gombosi, T. I., et al. (2015). Self-consistent multifluid MHD simulations of Europa’s exospheric interaction with Jupiter’s magnetosphere. *Journal of Geophysical Research: Space Physics*, 120, 3503–3524. <https://doi.org/10.1002/2015JA021149>
- Saur, J. (2004). A model of Io’s local electric field for a combined Alfvénic and unipolar inductor far-field coupling. *Journal of Geophysical Research*, 109(A1). <https://doi.org/10.1029/2002JA009354>
- Saur, J., Grambusch, T., Duling, S., Neubauer, F. M., & Simon, S. (2013). Magnetic energy fluxes in sub-Alfvénic planet star and moon planet interactions. *Astronomy and Astrophysics*, 552(A119), 1–20. <https://doi.org/10.1051/0004-6361/201118179>
- Saur, J., Neubauer, F. M., & Schilling, N. (2007). Hemisphere coupling in Enceladus’ asymmetric plasma interaction. *Journal of Geophysical Research*, 112(A11), A11209. <https://doi.org/10.1029/2007JA012479>
- Saur, J., Neubauer, F. M., Strobel, D. F., & Summers, M. E. (1999). Three-dimensional plasma simulation of Io’s interaction with the Io plasma torus: Asymmetric plasma flow. *Journal of Geophysical Research*, 104(A11), 25105–25126. <https://doi.org/10.1029/1999JA900304>
- Saur, J., Strobel, D. F., & Neubauer, F. M. (1998). Interaction of the Jovian magnetosphere with Europa: Constraints on the neutral atmosphere. *Journal of Geophysical Research*, 103, 19947–19962. <https://doi.org/10.1029/97JE03556>
- Schilling, N., Neubauer, F. M., & Saur, J. (2008). Influence of the internally induced magnetic field on the plasma interaction of Europa. *Journal of Geophysical Research*, 113, A03203. <https://doi.org/10.1029/2007JA012842>
- Simon, S. (2015). An analytical model of sub-Alfvénic moon-plasma interactions with application to the hemisphere coupling effect. *Journal of Geophysical Research: Space Physics*, 120, 7209–7227. <https://doi.org/10.1002/2015JA021529>
- Simon, S., Kriegel, H., Saur, J., & Wennmacher, A. (2013). Energetic aspects of Enceladus’ magnetospheric interaction. *Journal of Geophysical Research: Space Physics*, 118(6), 3430–3445. <https://doi.org/10.1002/jgra.50380>
- Simon, S., Kriegel, H., Saur, J., Wennmacher, A., Neubauer, F. M., Roussos, E., et al. (2012). Analysis of Cassini magnetic field observations over the poles of Rhea. *Journal of Geophysical Research*, 117(A7), A07211. <https://doi.org/10.1029/2012JA017747>
- Simon, S., Roussos, E., & Paty, C. S. (2015). The interaction between Saturn’s moons and their plasma environments. *Physics Reports*, 602, 1–65. <https://doi.org/10.1016/j.physrep.2015.09.005>
- Simon, S., Saur, J., Kriegel, H., Neubauer, F., Motschmann, U., & Dougherty, M. (2011). Influence of negatively charged plume grains and hemisphere coupling currents on the structure of Enceladus’ Alfvén wings: Analytical modeling of Cassini magnetometer observations. *Journal of Geophysical Research*, 116(A4), A04221. <https://doi.org/10.1029/2010JA016338>
- Simon, S., Saur, J., Neubauer, F., Motschmann, U., & Dougherty, M. (2009). Plasma wake of Tethys: Hybrid simulations versus Cassini MAG data. *Geophysical Research Letters*, 36(4), L04108. <https://doi.org/10.1029/2008GL036943>
- Simon, S., Saur, J., Neubauer, F. M., Wennmacher, A., & Dougherty, M. K. (2011). Magnetic signatures of a tenuous atmosphere at Dione. *Geophysical Research Letters*, 38, L15102. <https://doi.org/10.1029/2011GL048454>
- Simon, S., Saur, J., van Treeck, S. C., Dougherty, M. K., & Dougherty, M. K. (2014). Discontinuities in the magnetic field near Enceladus. *Geophysical Research Letters*, 41(10), 3359–3366. <https://doi.org/10.1002/2014GL060081>
- Simon, S., van Treeck, S. C., Wennmacher, A., Saur, J., Neubauer, F. M., Bertucci, C. L., & Dougherty, M. K. (2013). Structure of Titan’s induced magnetosphere under varying background magnetic field conditions: Survey of Cassini magnetometer data from flybys TA-T85. *Journal of Geophysical Research: Space Physics*, 118(4), 1679–1699. <https://doi.org/10.1002/jgra.50096>
- Volwerk, M., Khurana, K., & Kivelson, M. (2007). Europa’s Alfvén wing: Shrinkage and displacement influenced by an induced magnetic field. *Annales Geophysicae*, 25, 905–914. <https://doi.org/10.5194/angeo-25-905-2007>
- Zimmer, C., Khurana, K. K., & Kivelson, M. G. (2000). Subsurface Oceans on Europa and Callisto: Constraints from Galileo magnetometer observations. *Icarus*, 147(2), 329–347. <https://doi.org/10.1006/icar.2000.6456>